



**HAL**  
open science

## Modeling the growth of stylolites in sedimentary rocks

Alexandra Rolland, Renaud Toussaint, Patrick Baud, Jean Schmittbuhl,  
Nathalie Conil, Daniel Koehn, Francois Renard, Jean-Pierre Gratier

► **To cite this version:**

Alexandra Rolland, Renaud Toussaint, Patrick Baud, Jean Schmittbuhl, Nathalie Conil, et al.. Modeling the growth of stylolites in sedimentary rocks. 2012. hal-00701974

**HAL Id: hal-00701974**

**<https://hal.science/hal-00701974>**

Preprint submitted on 28 May 2012

**HAL** is a multi-disciplinary open access archive for the deposit and dissemination of scientific research documents, whether they are published or not. The documents may come from teaching and research institutions in France or abroad, or from public or private research centers.

L'archive ouverte pluridisciplinaire **HAL**, est destinée au dépôt et à la diffusion de documents scientifiques de niveau recherche, publiés ou non, émanant des établissements d'enseignement et de recherche français ou étrangers, des laboratoires publics ou privés.

# <sup>1</sup> Modeling the growth of stylolites in sedimentary <sup>2</sup> rocks.

Alexandra Rolland<sup>1,2</sup>, Renaud Toussaint<sup>1</sup>, Patrick Baud<sup>1</sup>, Jean Schmittbuhl<sup>1</sup>,  
Nathalie Conil<sup>2</sup>, Daniel Koehn<sup>3</sup>, François Renard<sup>4,5</sup>, Jean-Pierre Gratier<sup>4</sup>

---

Alexandra Rolland, Institut de Physique du Globe, Université de Strasbourg, 5 rue René Descartes, 67084 cedex, Strasbourg, France (alexandra.rolland@unistra.fr)

Renaud Toussaint, Institut de Physique du Globe, Université de Strasbourg, 5 rue René Descartes, 67084 cedex, Strasbourg, France (renaud.toussaint@unistra.fr)

Patrick Baud, Institut de Physique du Globe, Université de Strasbourg, 5 rue René Descartes, 67084 cedex, Strasbourg, France (patrick.baud@unistra.fr)

Jean Schmittbuhl, Institut de Physique du Globe, Université de Strasbourg, 5 rue René Descartes, 67084 cedex, Strasbourg, France (jean.schmittbuhl@unistra.fr)

Nathalie Conil, Agence Nationale pour la gestion des Déchets Radioactifs, Centre de Meuse/Haute-Marne, Route Départementale 960, BP 9, 55290, Bure, France

Daniel Koehn, University of Glasgow, Scotland

François Renard, ISTerre, Université Joseph Fourier, Grenoble, France

Jean-Pierre Gratier, ISTerre, Université Joseph Fourier, Grenoble, France

<sup>1</sup>Institut de Physique du Globe,

3 **Abstract.** Stylolites are ubiquitous pressure-solution seams found in sed-  
4 imentary rocks. Their morphology is shown to follow two self-affine regimes:  
5 analyzing the scaling properties of their height over their average direction  
6 shows that at small scale, they are self-affine surfaces with a Hurst exponent  
7 around 1, and at large scale, they follow another self-affine scaling with Hurst  
8 exponent around 0.5. In the present paper we show theoretically the influ-  
9 ence of the main principal stress and the local geometry of the stylolitic in-  
10 terface on the dissolution reaction rate. We compute how it is affected by  
11 the deviation between the principal stress axis, and the local interface be-  
12 tween the rock and the soft material in the stylolite. The free energy enter-  
13 ing in the dissolution reaction kinetics is expressed from the surface energy  
14 term, and via integration from the stress perturbations due to these local mis-  
15 alignments. The resulting model shows the interface evolution at different stress  
16 conditions. In the stylolitic case, i.e. when the main principal stress is nor-

---

Université de Strasbourg, France

<sup>2</sup>Andra, Bure, France

<sup>3</sup>School of Geographical and Earth  
Sciences, University of Glasgow, France

<sup>4</sup>ISTerre, University Joseph Fourier -  
Grenoble I and CNRS, France

<sup>5</sup>PGP, University of Oslo, Norway

17 mal to the interface, two different stabilizing terms dominate at small and  
18 large scales which are linked respectively to the surface energy and to the  
19 elastic interactions. Integrating the presence of small scale heterogeneities  
20 related to the rock properties of the grains in the model leads to the formu-  
21 lation of a Langevin equation predicting the dynamic evolution of the sur-  
22 face. This equation leads to saturated surfaces obeying the two observed scal-  
23 ing laws. Analytical and numerical analysis of this surface evolution model  
24 shows that the cross-over length separating both scaling regimes depends di-  
25 rectly on the applied far-field stress magnitude. This method gives the ba-  
26 sis for the development of a paleostress magnitude marker. We apply the com-  
27 putation of this marker, i.e. the morphological analysis, on a stylolite found  
28 in the Dogger limestone layer located in the neighborhood of the Andra Un-  
29 derground Research Laboratory at Bure (Eastern France). The results are  
30 consistent with the two scaling regimes expected, and the practical deter-  
31 mination of the major principal paleostress, from the estimation of a cross-  
32 over length, is illustrated on this example.

## 1. Introduction

33 Stylolites are undulated surfaces resulting from localized stress-driven dissolution of  
34 some minerals of the rock. Insoluble minerals as clay particles, oxides and organic mat-  
35 ters are concentrated in the interface and make stylolites visible. *Bathurst* [1987] describes  
36 stylolites as serrated interfaces with an amplitude greater than the diameter of the tran-  
37 sected grains giving them a sutured appearance. He makes a difference with dissolution  
38 seams or 'flaser' which are smooth, undulating, lacking in sutures and fitting around grains  
39 instead of cutting through them. Stylolites are most often found in carbonates [*Stock-*  
40 *dale*, 1922, 1926, 1936, 1943; *Dunnington*, 1954; *Bushinskiy*, 1961; *Park and Schot*, 1968;  
41 *Bathurst*, 1971; *Buxton and Sibley*, 1981; *Railsback*, 1993] but also in sandstones [*Young*,  
42 1945; *Heald*, 1955], shales [*Wright and Platt*, 1982; *Rutter*, 1983], cherts [*Bushinskiy*,  
43 1961; *Iijima*, 1979; *Cox and Whitford-Stark*, 1987] and sometimes in coal [*Stutzer*, 1940].  
44 Stylolites are divided in two groups according (i) to their orientation with respect to the  
45 bedding of the surrounding rock or (ii) to the orientation of their 'tooth' with respect to  
46 the mean plane of the stylolite. The first group shows two types of orientation: stylolites  
47 parallel to the bedding plane, designated as sedimentary, and formed under the lithostatic  
48 pressure and stylolites oblique or even perpendicular to the bedding, designated as tec-  
49 tonic, and depending on the maximum tectonic stress. The tooth orientation is in both  
50 cases an indicator of the direction of the incremental displacement which is parallel to  
51 the major principal stress in co-axial deformation. The stylolites of the second group are  
52 called 'slickolites' [*Ebner et al.*, 2010a]. They develop when there is a preferential plane  
53 for their growth (bedding or fracture). In this case, the stress is not perpendicular to the

54 mean plane of the stylolite [*Stockdale*, 1922], but the edges of the tooth are subparallel to  
55 the maximum principal stress axis. Various studies [*Park and Schot*, 1968; *Renard et al.*,  
56 1997, 2001; *André*, 2003; *Aharonov and Katsman*, 2009] suggest that many parameters  
57 play an important role in the stylolite growth such as confining pressure, deviatoric stress,  
58 fluid pressure, temperature, shape and assemblage of grains, anisotropy of minerals, rates  
59 of dissolution and presence of clay (acting potentially as catalyst for the dissolution).

60 Only few papers report experiments about stylolites development. Indeed, they are  
61 inherently difficult to reproduce as the kinetics of pressure-solution processes is very slow  
62 [*Rutter*, 1976]. Experiments were conducted either on aggregates [*Cox and Paterson*,  
63 1991; *Den Brok and Morel*, 2001; *Renard et al.*, 2001; *Gratier et al.*, 2005] or with in-  
64 denter techniques [*Gratier and Guiguet*, 1986; *Gratier*, 1993; *Gratier et al.*, 2004; *Dysthe*  
65 *et al.*, 2002, 2003; *Karcz et al.*, 2008]. *Dysthe et al.* [2002, 2003] used an indenter technique  
66 where a sodium chloride crystal was kept in contact with a piston at given pressure and  
67 temperature for several months. A fluid at compositional equilibrium with the crystal  
68 is trapped between the sample and the indenter. The contact evolved due to pressure-  
69 solution during the indentation. A power law time dependence with an exponent value of  
70  $1/3$  as in Andrade creep law was shown to control the indentation rate. The observed mi-  
71 crostructures in the contact seem to be different from stylolites. *Karcz et al.* [2008] loaded  
72 a halite cone-shaped indenter against a flat silicate surface immersed in an undersatu-  
73 rated brine. Using confocal microscopy techniques, they observed that the evolution of  
74 the system is dictated by an interaction between two deformation mechanisms: undercut-  
75 ting dissolution reducing the area of the contact and plastic flow increasing it. Recently,  
76 similar experiments were carried out with a brine at chemical equilibrium with the crystal

77 [*Laronne Ben-Itzhak*, 2011]. Emerging evolving islands and channels were observed at  
78 the contact. Such islands and channels structures were previously observed at the con-  
79 tacts during experiments on aggregates [*Schutjens and Spiers*, 1999; *Den Brok and Spiers*,  
80 1991]. Other experiments on aggregates were performed by *Gratier et al.* [2005]. They  
81 loaded layers of fine quartz sand grains. The experiments lasted several months at 350°C,  
82 under 50 MPa of differential stress and in presence of an aqueous silica solution. Microsty-  
83 lolites were created for the first time in the laboratory at the stressed contacts between the  
84 quartz grains. An interesting observation is that the stylolites peaks are always located  
85 in front of dislocation pits. Consequently, stylolites appear to be localized by the hetero-  
86 geneities of the mineral. *Den Brok and Morel* [2001] loaded elastically K-alum crystals at  
87 a controled temperature and in a saturated K-alum solution. A hole was drilled in the  
88 middle of the crystals to provide an elastic strain gradient. They observed macroscopic  
89 etch grooves on the originally smooth free surfaces of the soluble crystals which disappear  
90 when removing the stress. *Koehn et al.* [2004] stressed crystals of  $NaClO_3$  in a  $NaClO_3$   
91 solution at room temperature. Parallel dissolution grooves developed on their free surface  
92 in a 1D geometry to a 2D geometry with the coarsening of the pattern. The pressure-  
93 solution process slowed down or stopped progressively with the increasing concentration  
94 of the solution during the experiments. *Gratier et al.* [2004] used a similar technique in  
95 which a sample of Bure claystone was kept in contact with a piston, with a saturated  
96 brine in the contact, at an imposed pressure and temperature for several months. No  
97 evidence of localized pressure-solution (dissolution seam) was observed in this case, grain  
98 to grain sliding being more efficient in presence of clay. *Renard et al.* [2001], studied  
99 chemical compaction of aggregates of halite (salt) mixed with clay. They showed that

100 clay particles enhance pressure-solution. Moreover, *Renard et al.* [1997] studied the effect  
101 of clay on clay-rich sandstones. They suggested that pressure-solution is enhanced by clay  
102 because a thick film of water is preserved between clay particles. They also concluded  
103 that the depth determines the limiting factor for the process: at great depth, the water  
104 film between grains should be thinner and diffusion limits the process. Conversely, at low  
105 depth water films are bigger, transport is easier and the reaction kinetics is the limiting  
106 factor.

107 The clay particles effect on pressure-solution was recently simulated in numerical mod-  
108 eling. *Aharonov and Katsman* [2009] used the two-dimensional Spring Network Model to  
109 study the stylolites growth in a medium with a uniform clay distribution. They showed  
110 that clay plays a role of enhancing pressure-solution and that stylolites propagation is  
111 possible only when both pressure-solution and clay-enhanced dissolution operate together.  
112 *Koehn et al.* [2007] developed a new discrete simulation technique that reproduces suc-  
113 cessfully the roughening of stylolites from a preferential existing surface with no clay. This  
114 model is based on molecular dynamics, with a dissolution speed depending on the local  
115 free energy that includes stress dependent terms and surface energy terms. Two different  
116 spatial regimes arise from this modeling: a small-scale regime where surface energy is  
117 dominant with significant fluctuations of the roughness and a large-scale regime where  
118 elastic energy dominates. The dependence on the cross-over scale between both regime  
119 on the imposed stress has been recently investigated numerically [*Koehn*, 2012]. This  
120 model shows that the growth of the stylolite tooth follows the main compressive stress  
121 direction. The nature and structure of the small scale disorder for the dissolution prop-  
122 erties of grains were systematically analyzed [*Ebner et al.*, 2009a]. Moreover, *Ebner et al.*

123 [2010b] performed detailed microstructural analysis to investigate the interplay between  
124 this disorder and the compositional nature of the grains surrounding a stylolite.

125 Stylolites are localised features for which deformation is purely compactant as for com-  
126 paction bands [*Mollema and Antonellini, 1996; Baud et al., 2004; Katsman et al., 2006b;*  
127 *Tembe et al., 2008*]. Stylolites and compaction bands development was modeled as ant-  
128 icracks or anti-mode I fracture [*Fletcher and Pollard, 1981; Rispoli, 1981; Mollema and*  
129 *Antonellini, 1996*]. *Fletcher and Pollard [1981]* assume that the rate of pressure-solution  
130 is only a function of the normal stress. They observed an elliptic dissolution pattern i.e.  
131 more dissolution in the central part of stylolites than at the tips. With these observations  
132 they proposed an analogy between propagation of stylolites and propagation of mode I  
133 fractures. They observed that the relative displacement between the sides of a stylolite  
134 should have the opposite sign than that of a crack, and thus termed their model an an-  
135 ticrack. Note however that cracks can bear zero surface traction, contrary to stylolites.  
136 This distinction between crack solutions and stylolites was introduced, and it was shown  
137 by *Katsman et al. [2006a]* that, as compaction bands, stylolites are Localized Volume  
138 Reduction zones (LVR). The shape of the displacement along stylolites, and how the  
139 stress perturbation can be determined from the concept of LVR, is discussed in details by  
140 *Katsman [2010]*.

141 In LVR where the dissolution amount is constant across the surface of the LVR, as for a  
142 compaction band, the stress enhancement was shown to be that of a dislocation [*Katsman*  
143 *et al., 2006a*]. In later models *Katsman [2010]*, it was shown that if more dissolution is  
144 allowed in the center of a stylolite, another type of stress enhancement, with a dependence  
145 on the distance to the tips analogous to the one for a crack (rather than to a dislocation),

146 can be observed it is given by the Eshelby inclusion problem. Such an increase of the  
147 dissolution in the center of a stylolite, where the dissolution does not stop in the already  
148 dissolved zone in the middle of the stylolite, can be observed in models with a positive  
149 feedback do the dissolution, as for example the one that can be modeled from a clay  
150 concentration mechanism [*Aharonov and Katsman, 2009*].

151 In general, in stylolites, the stress concentrates at the tips and the largest stress is  
152 perpendicular to the stylolites. Recent models [*Koehn et al., 2007; Ebner et al., 2009b;*  
153 *Zhou and Aydin, 2010*] suggest that a higher stress concentration at the top of the tooth  
154 should be responsible of localized high rates of dissolution. *Benedicto and Schultz [2010]*  
155 investigated the topography of stylolites (along-strike trace length, maximum and average  
156 amplitudes) from the damaged zone of the Gubbio normal fault zone in central Italy. They  
157 showed that the amount of contractional strain accommodated by stylolites as well as their  
158 length and their number increase according to the topography parameters. Analyses of  
159 cores from boreholes reveal also an increase in stylolite abundance with depth [*Lind,*  
160 *1993*]. *Fabricius and Borre [2007]* compared formations of chalk from boreholes on the  
161 Ontong Java Plateau and in the central North Sea. They showed that the burial stress  
162 and the temperature play distinct roles in the burial diagenesis and porosity development  
163 of chalk. Pressure-solution and physical compaction are controlled by the burial stress  
164 while the temperature controls recrystallization and cementation. Moreover, *Lind [1993]*  
165 suggests that mineralogical anomaly is an initializing factor in stylolite formation such as  
166 burrows, shale clasts or flaser structures. Many studies were conducted on the morphology  
167 of sedimentary stylolites [*Renard et al., 2004; Brouste et al., 2007; Ebner et al., 2009b*].  
168 Morphology analyses can be done on 1D profiles or 2D opened surfaces. They consist

169 on studying a stylolitic profile or surface height variations (standard deviation, height  
170 differences, power spectrum, average wavelet coefficient spectrum, etc.) over different  
171 scales [*Schmittbuhl et al.*, 1995, 2004; *Renard et al.*, 2004]. These analyses reveal two  
172 distinct scaling regimes that could be described by power laws. The power laws are  
173 function of a roughness exponent also called Hurst exponent inferred to be 1 and 0.5 for  
174 small and large scale respectively [*Renard et al.*, 2004; *Schmittbuhl et al.*, 2004; *Brouste*  
175 *et al.*, 2007; *Ebner et al.*, 2009b]. The two regimes are separated by a cross-over length  
176 typically around 1 mm [*Renard et al.*, 2004; *Schmittbuhl et al.*, 2004]. For sedimentary  
177 stylolites, the two dimensional (2D) analysis of their surface does not show any significant  
178 inplane anisotropy reflecting the fact that horizontal stresses are isotropic. *Ebner et al.*  
179 [2010a] observed that the profiles of tectonic stylolites show the same geometric attributes  
180 as sedimentary ones. Two different regimes are also observed with Hurst exponent around  
181 1 and 0.5 for small and large scale respectively. However, for tectonic stylolites, the 2D  
182 analysis revealed an anisotropy of the cross-over length which varies with the direction in  
183 the plane of stylolites. *Ebner et al.* [2010a] argue that this anisotropy develops because  
184 the stylolite roughens in an anisotropic inplane stress field. The vertical and inplane  
185 horizontal stresses are significantly different. In recent papers, stylolites are presented as  
186 fossilized signatures of the stress field [*Renard et al.*, 2004; *Schmittbuhl et al.*, 2004; *Ebner*  
187 *et al.*, 2009b, 2010a]. The existence of two scaling regimes for sedimentary stylolites was  
188 shown in *Schmittbuhl et al.* [2004] where a brief theoretical derivation was performed.  
189 It was shown that the cross-over length between both scaling regimes is expected to  
190 be dependent on the stress acting on the stylolite during its growth. Their conclusion  
191 was that stylolite morphology can be used as a paleostress magnitude indicator. This

192 conclusion was later probed independently on two types of approaches: first, on field data  
193 sampled from the same formation at different heights, *Ebner et al.* [2009b] showed that the  
194 measured cross-over length in the morphology followed the expected scaling with the burial  
195 stress, evaluated from the position in the formation. Next, discrete numerical simulations  
196 were carried out at different stress magnitudes, allowing for the dissolution of grains along  
197 the fluid/rock interface, with free energy depending on interfacial tension and local stress.  
198 It was shown that the two expected scaling regimes were observed [*Koehn et al.*, 2007;  
199 *Koehn*, 2012], and that the cross-over length followed the predicted dependence on the  
200 far-field stress amplitude [*Koehn*, 2012].

201 Interfaces between solids and fluids are related to models of stylolitization. In the case  
202 where a solid in contact with a fluid is stressed, an instability due to pressure-solution  
203 was shown theoretically to exist and is called the Asaro-Tiller-Grinfeld (ATG) instability  
204 [*Renard et al.*, 2004]. In models of dissolving surfaces with a stress imposed to a solid in  
205 contact with a fluid at chemical equilibrium, this instability leads to the growth of initial  
206 large scale modulations of the surface with a wavelength selection obtained through a  
207 fastest growing mode. The basic equation depends on the particular boundary conditions  
208 e.g. when two solids with different elastic properties are in contact and submitted to a  
209 stress, the interface can undergo a fingering instability led by the contrast between the  
210 free energies applied to both solids [*Angheluta et al.*, 2008, 2009, 2010]. The stability  
211 analysis can be performed theoretically from expressions for the kinetics using local free  
212 energy criteria for the reaction rate [*Renard et al.*, 2004; *Schmittbuhl et al.*, 2004], or  
213 global ones [*Bonnetier et al.*, 2009; *Angheluta et al.*, 2008]. Depending on the boundary  
214 conditions, this situation is also found to be unstable for perturbations exceeding a certain

215 wavelength, leading to fingering (as e.g. with large stress tangential to a fluid interface,  
216 or a stress normal to fluid interfaces and lateral periodic boundary conditions [*Bonnetier*  
217 *et al.*, 2009]). With other boundary conditions, the surface energy and elastic interactions  
218 are found to stabilize the interfaces, which are only destabilized by material noise due to  
219 heterogeneities [*Schmittbuhl et al.*, 2004; *Koehn et al.*, 2007]. We will argue in details in the  
220 discussion section about the different possibilities applied to the geometry of stylolites,  
221 and the fact that stylolites displaying self-affine scaling laws for their height at large  
222 scale are compatible with the stabilizing character of elastic forces at large scale. This  
223 manuscript provides the technical development and details that lead to the final result  
224 that was previously published without derivation, in a condensed form [*Schmittbuhl et al.*,  
225 2004]. It also compares the result of the analytical development to a direct numerical  
226 simulation.

227 In this paper we concentrate on the following questions: (i) Is the elastic energy sta-  
228 bilizing or destabilizing? (ii) What is the significance of the obtained paleostress values?  
229 To answer to these questions, (i) we derive the details of the computation leading to the  
230 link between the paleostress magnitude and the cross-over length between the two scaling  
231 regimes. This is performed by a perturbative analysis of the elastic energy around an  
232 interface slightly wavy and unaligned with one of the principal stresses. Then we show in  
233 details that the mechanics and chemistry allow to relate the small and large scale behavior  
234 of stylolites to known models, with Hurst exponents corresponding to the observed ones.  
235 (ii) We finally present and discuss an application in relation with the geological context.  
236 This is made on a stylolite from the Bure carbonates and it shows how the predicted

237 scaling regimes can be found, and how to determinate the paleostress from the extracted  
238 cross-over length.

## 2. Analytical approach : Continuous elastostatic model for stylolite propagation

239 The rough morphology of stylolites arises from the disorder present in a rock and its  
240 impact on the pressure-solution process. This disorder is spatially linked to the grains con-  
241 stituting the rock. To understand the impact of this disorder on the chemico-mechanical  
242 coupling, we will consider the following simplified geometry: the initial stage of the sty-  
243 lolite is modeled as an elongated fluid pocket enclosed between two contactless rough  
244 surfaces of infinite extent. The contacts between these two surfaces can in principle mod-  
245 ify the geometry of the resulting dissolution surface. However, they are assumed to be  
246 sufficiently loose in a stylolite and thus the main morphological results are not affected.  
247 This assumption simplifies the problem since the dissolution process, happening on both  
248 sides of the stylolite (Figure 1), can be described as the dissolution of a solid half-plane in  
249 contact with a fluid. With this geometry, the small and large scale self-affine behaviors of  
250 the dissolution surface and the associated roughness exponents (or Hurst exponents) are  
251 well reproduced. The model leads to the characteristic exponents typically observed in  
252 previous studies [*Renard et al.*, 2004; *Schmittbuhl et al.*, 2004; *Brouste et al.*, 2007; *Ebner*  
253 *et al.*, 2009b].

254 The average stylolitic plane is defined along the  $x$  and  $y$ -axis (Figure 2). To have  
255 better statistics on the morphology of the studied surfaces, the model is assumed to be  
256 invariant by translation along the  $y$ -axis. It allows to us to describe a larger range of  
257 scales at the same numerical cost and to numerically solve the self-affine behavior of the

258 resulting pressure-solution surface over a larger number of orders of length scales. The  
259 same approach can be considered using invariance by translation along the  $x$ -axis. In  
260 the model we assume a mechanical equilibrium throughout the system and express the  
261 dissolution rate as a function of the stress tensor and of the area of interface per unit  
262 volume.

## 2.1. Force perturbation related to the mechanical equilibrium along the fluid-solid interface

263 First, we express the mechanical equilibrium at the solid-fluid interface (Figure 2).  
264 The convention adopted is that compressive stresses and compactive strains are negative  
265 *Landau and Lifchitz* [1986]. The far-field stress applied to the host rock is denoted by  
266  $\bar{\sigma}^0$ . The largest principal stress axis, perpendicular to the average plane of the stylolite,  
267 is defined along the  $z$ -axis. The fluid pocket transmits all the load through itself (The  
268 boundary condition of the fluid pocket is approximated as undrained for that respect:  
269 if there is any flow, from or into the fluid pocket, it happens slowly, via the lateral  
270 ends. If there is any contact between the opposite walls perpendicular to the main fluid  
271 direction, the load transmitted through this contact is neglected). The fluid pressure  
272 is thus homogeneous and equal to the largest principal stress applied to the host rock,  
273 considering the integral of the local stress field  $\bar{\sigma}$  along an elongated rectangular boundary  
274 (dashed line in Figure 1):

$$275 \quad p = -\sigma_{zz}^0 \quad (1)$$

276 Locally, the local stress  $\bar{\sigma}$  is split between the far-field asymptotic value  $\bar{\sigma}^0$  and a pertur-  
277 bation generated by the irregular nature of the interface  $\bar{\sigma}^1$ :

$$278 \quad \bar{\sigma}(x) = \bar{\sigma}^0 + \bar{\sigma}^1(x) \quad (2)$$

279 The far-field stress unit vectors  $\hat{x}$  and  $\hat{z}$  along the  $x$  and  $z$ -axis are assumed to be the  
 280 principal directions i.e.

$$281 \quad \bar{\sigma}^0 = \sigma_{xx}^0 \hat{x}\hat{x} + \sigma_{zz}^0 \hat{z}\hat{z} \quad (3)$$

282 Here, the notations  $\hat{x}\hat{x}$  and  $\hat{z}\hat{z}$  correspond to unit matrixes composed from the unit  
 283 vectors, as e.g. are  $\hat{y}\hat{y}$ ,  $\hat{x}\hat{y}$ , or  $\hat{z}\hat{x}$ . This canonical basis for the matrixes is composed  
 284 from the doublets of unit vectors  $\hat{x}, \hat{y}$  and  $\hat{z}$ . For example,  $\hat{x}\hat{z}$  represents the unit matrix  
 285 with all components equal to zero, apart from a unit in the lign corresponding to the  $x$   
 286 coordinate, and the column corresponding to the  $z$  one, so that for a pair of vectors  $u, v$   
 287 applied to the left and right of this matrix,  $u \cdot (\hat{x}\hat{z}) \cdot v = (u \cdot \hat{x})(\hat{z} \cdot v) = u_x v_z$ . In other  
 288 terms, with cartesian components along directions of indexes  $i$  and  $j$ , and the help of the  
 289 Kronecker symbol  $\delta$ , the components of the matrix  $\hat{x}\hat{z}$ , for example, are:  $(\hat{x}\hat{z})_{ij} = \delta_{ix}\delta_{jz}$ .  
 290 This convention to define the canonical basis of matrix space (nine elementary second  
 291 order dyadic products like  $\hat{x}\hat{z}$ ) from the three basic unitary vectors of the vectorial space,  
 292  $\hat{x}, \hat{y}$  and  $\hat{z}$  is, for example, defined by [Gonzalez and Stuart, 2008].

293 For a stylolite, the largest compressive stress axis is normal to its average plane and  
 294 thus to the average fluid pocket direction:

$$295 \quad |\sigma_{zz}^0| > |\sigma_{xx}^0| \quad (4)$$

296 This relation has strong implications on the stability of the surface pattern emerging from  
 297 the dissolution process. The far-field deviatoric stress is defined as:

$$298 \quad \sigma_s^0 = (|\sigma_{zz}^0| - |\sigma_{xx}^0|) = (\sigma_{xx}^0 - \sigma_{zz}^0) \quad (5)$$

299 To express the force perturbation related to the curved nature of the interface, we define  
 300 the unit vector  $\hat{n}$  normal to the surface pointing towards the fluid. This vector is assumed

301 to be close to the principal stress axis. In the following, we will consider small-angle devia-  
 302 tions from a straight surface, and the results will therefore be valid for small surface slopes  
 303 only. The model presented below aims to describe the onset of the stylolite propagation  
 304 from a flat surface, and it will also describe the evolution of large wavelength modes, if  
 305 the aspect ratio of such modes (ratio of the amplitude over the wavelength) stays small,  
 306 corresponding to small effective slopes at large wavelength.

307 The interface is described as a single-valued function  $z(x)$  and the slopes are assumed to  
 308 be of the order  $\epsilon$  i.e. that  $|\partial_x(z)| \in O(\epsilon) \ll 1$ . Since the normal  $\hat{n}$  to the interface of slope  
 309  $\partial_x z$  can be expressed by the conditions of normality to the interface,  $\hat{n} \cdot (1, \partial_x z)^T = 0$   
 310 (at any order or  $\epsilon$ ), and by its unitary norm  $\hat{n}^2 = 1$ , it is in general  $\hat{n} = (-(\partial_x z)\hat{x} +$   
 311  $\hat{z})/\sqrt{1 + (\partial_x z)^2}$ . Using the above limit of small slopes, developing in  $\epsilon$ , we obtain to  
 312 leading order

$$313 \quad \hat{n} = \hat{z} - (\partial_x z)\hat{x} + O(\epsilon^2) \quad (6)$$

314 (The order  $O(\epsilon)$  is absent from  $\hat{n}$ ).

315 The local mechanical equilibrium at the solid-fluid interface is expressed as:

$$316 \quad \sigma \cdot \hat{n} = -p\hat{n} \quad (7)$$

317 And with equations (1-7) the force perturbation (illustrated in Figure 3) becomes:

$$318 \quad \delta f(x) = \sigma^1(x) \cdot \hat{n} =$$

$$319 \quad -p\hat{n} - \sigma^0 \cdot \hat{n}$$

$$320 \quad = \sigma_{zz}^0[\hat{z} - (\partial_x z)\hat{x}] - \sigma_{zz}^0\hat{z} + \sigma_{xx}^0(\partial_x z)\hat{x}$$

$$321 \quad = (\sigma_{xx}^0 - \sigma_{zz}^0)(\partial_x z)\hat{x}$$

$$322 \quad = \sigma_s^0(\partial_x z)\hat{x} \quad (8)$$

## 2.2. Chemico-mechanical coupling

323 Next, we express the chemico-mechanical coupling. The dissolution speed normal to the  
324 solid/fluid interface (in  $\text{mol}\cdot\text{m}^{-2}\cdot\text{s}^{-1}$ ), is to the first order proportional to the chemical  
325 potential  $\Delta\mu$  of the chemical product dissolving [*Kassner et al.*, 2001; *Misbah et al.*, 2004;  
326 *Schmittbuhl et al.*, 2004; *Koehn et al.*, 2007]:

$$327 \quad v = m\Delta\mu \quad (9)$$

328 where

$$329 \quad m = k_0\Omega/RT \quad (10)$$

330 is the mobility of the dissolving species,  $R = 8.31 \text{ J}\cdot\text{mol}^{-1}\cdot\text{K}^{-1}$  is the universal gas  
331 constant,  $T$  is the temperature in Kelvin,  $k_0$  is a dissolution rate which can be measured  
332 experimentally, and  $\Omega$  is a molar volume. For calcite,  $\Omega \simeq 4\cdot 10^{-5} \text{ m}^3\cdot\text{mol}^{-1}$  and  $k_0 \simeq 10^{-4}$   
333  $\text{mol}\cdot\text{m}^{-2}\cdot\text{s}^{-1}$  for dissolution in water at atmospheric pressure and 298°K [*De Giudici*, 2002;  
334 *Schmittbuhl et al.*, 2004]. The difference in chemical potential from the solid state to the  
335 fluid state is [*Kassner et al.*, 2001; *Misbah et al.*, 2004; *Koehn et al.*, 2007]:

$$336 \quad \Delta\mu = \Delta\Psi_s + \Omega\Delta P_n + \Omega\gamma\kappa \quad (11)$$

337 Considering a solid state at given pressure and elastic free energy in chemical equilibrium  
338 with the fluid,  $\Delta\Psi_s$  and  $\Delta P_n$  are defined respectively as the change in Helmholtz free energy  
339 per mole and the change in stress normal to the interface. The last term corresponds to the  
340 surface energy with  $\kappa = \partial_{xx}z$ , the surface curvature (the inverse of the radius curvature)  
341 and  $\gamma$  the surface tension between the solid and the fluid phase. In a particular case,  
342 neglecting temperature variation effects and assuming that the fluid composition is in  
343 chemical equilibrium with a solid flat surface at normal pressure  $p$  and stress  $\sigma_{ref}$ , Eq.(11)

344 reduces to :

$$345 \quad \Delta\mu = 0 \quad (12)$$

$$346 \quad \kappa = 0 \quad (13)$$

347 More generally, by definition ([*Kassner et al.*, 2001]:

$$348 \quad \Delta\Psi_s + \Omega\Delta P_n = \Omega\Delta u_e, \quad (14)$$

349 where

$$350 \quad \Delta u_e = u_e(\sigma) - u_e^{ref} \quad (15)$$

351 and

$$352 \quad u_e = [(1 + \nu)\sigma_{ij}\sigma_{ij} - \nu\sigma_{kk}\sigma_{ll}]/4E \quad (16)$$

353 is the elastic free energy per unit volume with  $E$  the Young's modulus and  $\nu$  the Poisson's  
354 ratio of the elastic solid [*Kassner et al.*, 2001; *Landau and Lifchitz*, 1986].

355 To take into account the dissolution speed variations associated to the morphology of  
356 the stylolite, we develop the dissolution speed to the leading order as:

$$357 \quad v = v^0 + v^1 \quad (17)$$

358 With equations (9-16):

$$359 \quad v^0 = \frac{k_0\Omega^2}{RT} \left( \frac{[(1 + \nu)\sigma_{ij}^0\sigma_{ij}^0 - \nu\sigma_{kk}^0\sigma_{ll}^0]}{4E} - u_e^{ref} \right) \\ 360 \quad = \frac{k_0\Omega^2}{RTE} (\alpha p_0^2 - \alpha_{ref} p_{ref}^2) \quad (18)$$

361 The geometrical factor  $\alpha$  is computed assuming  $\sigma_{xx}^0 = \sigma_{yy}^0 = -p_0 + \sigma_s/3$  and  $\sigma_{zz}^0 =$   
362  $-p_0 - 2\sigma_s/3$ :

$$363 \quad \alpha = \frac{9(1 - 2\nu) + 2(1 + \nu)\sigma_s^2/p_0^2}{\text{March 31, 2012, 6:14pm}} \quad (19)$$

364  $\alpha_{ref}$  is expressed with a similar expression and characterizes the chemical equilibrium with  
365 the fluid at the referential state as a function of the pressure  $p_{ref}$  and the shear stress  
366  $\sigma_{ref}$ . Typically, for a limestone with a Young's modulus  $E = 80$  GPa stressed at  $p_0 \simeq 10$   
367 MPa (which corresponds to a few hundred of meters deep in sedimentary rocks) and for a  
368 fluid with a chemical composition in equilibrium with the solid, the dissolution speed at  
369 the solid-fluid interface in a limestone is of the order of:

$$370 \quad v_n^0 \simeq 10^{-6} \text{ to } 10^{-5} \text{ m.year}^{-1}$$

### 2.3. Consequences for the stability of the dissolution process

371 From the local mechanical equilibrium and the nature of the chemico-mechanical cou-  
372 pling, some important considerations can be inferred about the morphological stability of  
373 the dissolution surfaces. This behavior depends on the orientation of the surfaces with  
374 respect to the far-field stress.

375 Previously we have shown how to express the force perturbation arising from the mis-  
376 match between the solid-fluid interface orientation and the principal axis of the far-field  
377 stress tensor  $\hat{x}$  (equation 8).

378 This relationship holds independently of the relative magnitudes of the principal stresses  
379  $\sigma_{xx}$  and  $\sigma_{zz}$ . If the largest principal stress is tangential to the interface, which is not the  
380 case for stylolites,  $\sigma_s^0 < 0$  and the sign of  $\delta f(x) \cdot \hat{x}$  is opposite to the slope of the interface  
381  $\partial_x z$ . Such tangential force perturbation is concentrated at the points lying ahead of the  
382 average dissolution front (Figure 4). The elastic forces concentrate stress at the valleys of  
383 the dissolution front where the free energy is thus higher. This leads to an increased dis-  
384 solution speed at the points lying ahead of the averaged front. The dissolution propagates  
385 downwards. The points at the crests, i.e. located behind the averaged dissolution front,

386 show a reduced rate of dissolution thus pushing them further from the average front. The  
387 points lying out of the average dissolution plane tend therefore to depart further from  
388 the average position. The elastic force is in this situation a destabilizing force. On the  
389 contrary, the surface tension tends to stabilize the process by decreasing the surface area  
390 by flattening the interface.

391 The competition between the elastic long-range destabilizing forces and the surface  
392 tension short-range stabilizing forces leads to the ATG interface instability. The fastest  
393 growing wavelength is determined by the balance between these long-range destabilizing  
394 and short-range stabilizing effects. Such instability arising in stressed solids was studied  
395 theoretically [*Asaro and Tiller, 1972; Grinfeld, 1986; Misbah et al., 2004*] and observed  
396 experimentally in stressed soluble crystals immersed in a saturated fluid [*Den Brok and*  
397 *Morel, 2001; Koehn et al., 2004*].

398 If the largest principal stress lies perpendicular to the interface, as for stylolites,  $\sigma_s^0 > 0$   
399 and the sign of  $\delta f(x) \cdot \hat{x}$  is the same as the slope of the interface  $\partial_x z$ . Such tangential  
400 force perturbation is concentrated at the points lying behind of the average dissolution  
401 front (Figure 5). The elastic forces concentrate stress at the crests of the dissolution front  
402 where the free energy is thus higher. This leads to an increased dissolution speed for  
403 the points lying behind the averaged front. The dissolution propagates downwards. The  
404 points at the valleys, i.e. located ahead of the averaged dissolution front, tend to come  
405 back to the average position. The elastic force is a stabilizing force in this situation. Here,  
406 the surface tension is again a stabilizing process.

407 Since the long-range elastic force and the short-range surface tension force are stabilizing  
408 forces, if the modeled solid properties are purely homogeneous (i.e. homogeneous elastic

409 solid with homogeneous dissolution rate properties), the model predicts the flattening of  
410 any initial non-plane surface with time.

411 Consequently, to model the morphogenesis of stylolites, which are rough surfaces, we  
412 will take here into account the disorder linked to the material properties.

### 413 **2.3.1. Consequence on initial evolution of trapped fluid pocket**

414 In summary, the above arguments show that an elementary bump of a flat surface dis-  
415 appears for  $\sigma_s > 0$ , or grows for  $\sigma_s < 0$ . Qualitatively, if the argument on the stability  
416 of surfaces depending on their orientation on the principal stress axis extends for more  
417 local orientations along trapped fluid pockets, one should observe the following: for the  
418 sides of a fluid pocket lying tangentially to the largest stress, these should develop instable  
419 grooves penetrating into the solid, similarly to the ATG instability case. On the contrary,  
420 the sides normal to the largest stress direction should remain relatively flat, apart from  
421 the fluctuations due to the disorder. These small variations along the surfaces normal to  
422 the principal stress axis, and the penetrations of grooves of characteristic wavelength in  
423 the rock along the direction of the weakest stress, should lead to the development of elon-  
424 gated structures, and merge initially separated fluid pockets (or clay-enriched pockets).  
425 This qualitative mechanism is illustrated on Figure 6. This expectation of qualitative  
426 evolution is indeed compatible with the mechanism of development of anti-cracks numer-  
427 ically obtained by *Koehn et al.* [2003]. The experimental grooves observed along the free  
428 surface on the sides of a fluid-filled cylindrical pocket by *Den Brok and Morel* [2001] also  
429 displayed this trend.

## 2.4. Expression of the dissolution speed perturbation as a function of the interface shape

430 To model the disorder in the solid we assume that the material properties (related to the  
 431 solid grains) vary in a random and spatially uncorrelated way. This disorder can originate  
 432 from the diversity of grain composition, grain size or orientation, i.e. it represents the  
 433 small scale heterogeneities present in the rock For example, the dissolution rate  $k$  can be  
 434 expressed as an averaged term  $k_0$  plus some spatial variations of zero average  $\eta(x, z) \cdot k_0$ :

$$435 \quad k = k_0(1 + \eta(x, z(x))) \quad (20)$$

436 The random variable  $\eta$  is a quenched disorder with no spatial correlations and is charac-  
 437 terized by its mean  $\langle \eta \rangle = 0$  and its variance  $\langle \eta^2 \rangle$  assumed to be small enough to  
 438 keep small local slopes. The dynamics of the dissolving interface  $z(x, t)$  can be expressed  
 439 from equations (9-17) as:

$$440 \quad v = -\partial_t z = \frac{k\Omega^2}{RT}(\Delta u_e + \gamma\partial_{xx}z),$$

$$441 \quad = \frac{k_0\Omega^2}{RT}(1 + \eta)\{(1 + \nu)[(\sigma_{ij}^0 + \sigma_{ij}^1)(\sigma_{ij}^0 + \sigma_{ij}^1) - \nu(\sigma_{kk}^0 + \sigma_{kk}^1)^2]/4E - u_{ref}^e + \gamma\partial_{xx}z\}$$

$$442 \quad = \frac{k_0\Omega^2}{RT}\{(1 + \nu)[\sigma_{ij}^0\sigma_{ij}^0 - \nu(\sigma_{kk}^0)^2]/4E - u_{ref}^e\}$$

$$443 \quad + \frac{k_0\Omega^2}{RT}\eta\{(1 + \nu)[\sigma_{ij}^0\sigma_{ij}^0 - \nu(\sigma_{kk}^0)^2]/4E - u_{ref}^e\}$$

$$444 \quad + \frac{k_0\Omega^2}{RT}\{(1 + \nu)[2\sigma_{ij}^0\sigma_{ij}^1 - 2\nu(\sigma_{kk}^0\sigma_{kk}^1)]/4E + \gamma\partial_{xx}z\} \quad (21)$$

445 i.e., using Eq.(18) for the expression of  $\sigma_{ij}^0\sigma_{ij}^0 - \nu(\sigma_{kk}^0)^2$ , a dissolution speed separated  
 446 between an average homogeneous speed  $v_0$  and a leading order of the perturbations  $v_1$ ,  
 447 first order in  $\epsilon$  as

$$448 \quad \partial_t z(x, t) = -v_0 - v_1(x, t) \quad (22)$$

449 with  $v_0$  the dissolution speed given by equation (18) and  $v_1$  a deviation of the dissolution  
 450 speed with respect to the average dissolution speed  $v_0$  expressed as:

$$\begin{aligned}
 451 \quad v^1 &= \frac{k_0 \Omega^2}{RT} \frac{(\alpha p_0^2 - \alpha_{ref} p_{ref}^2)}{E} \eta(x, z(x)) \\
 452 \quad &+ \frac{k_0 \Omega^2}{RT} \gamma \partial_{xx} z(x) \\
 453 \quad &+ \frac{k_0 \Omega^2}{RT} \left( \frac{[(1 + \nu) \sigma_{ij}^0 \sigma_{ij}^1 - \nu \sigma_{kk}^0 \sigma_{ll}^1]}{2E} \right) \tag{23}
 \end{aligned}$$

454  $\sigma^1$  is the stress perturbation mentioned previously in equation (2). It is generated by the  
 455 surface distribution of the tangential force perturbation  $\delta f(x)$  due to the irregular nature  
 456 of the interface.

457 The first term is a quenched disorder term leading to the roughening of the interface.  
 458 The second one is a stabilizing quadratic short-range term arising from the surface tension.  
 459 The last term can be expressed via a non-local kernel from the shape of the interface  $z(x)$   
 460 by integrating the elastostatic equations in the solid half-plane.

## 2.5. Detailed form of the elastic long-range interaction kernel

461 The stress perturbation induced by the force perturbation  $\delta f(x)$  (equation 8) exerted  
 462 on the surface can be determined via the Green function method. Following *Landau and*  
 463 *Lifchitz* [1986], the displacement induced by an elementary force  $\hat{x}$  applied at the origin  
 464  $(0, 0, 0)$  on a semi-infinite solid is:

$$\begin{aligned}
 465 \quad a_x(x, y, z) &= \frac{1 + \nu}{2\pi E} \left\{ \frac{2(1 - \nu)r + z}{r(r + z)} + \frac{(2r(\nu r + z) + z^2)}{r^3(r + z)^2} x^2 \right\} \\
 466 \quad a_y(x, y, z) &= \frac{1 + \nu}{2\pi E} \left\{ \frac{2r(\nu r + z) + z^2}{r^3(r + z)^2} xy \right\} \\
 467 \quad a_z(x, y, z) &= \frac{1 + \nu}{2\pi E} \left\{ \frac{(1 - 2\nu)x}{r(r + z)} + \frac{zx}{r^3} \right\} \tag{24}
 \end{aligned}$$

468 where  $r$  is the distance relatively to the force application point at  $(0,0,0)$ , i.e.  $r^2 =$   
 469  $x^2 + y^2 + z^2$ . The associated strain applied on the solid is:

$$470 \quad \epsilon_{ij}^e = \frac{1}{2}(\partial_i a_j + \partial_j a_i) \quad (25)$$

471 and the associated stress is:

$$472 \quad f_{ij}(x, y, z) = \frac{E}{1 + \nu}(\epsilon_{ij}^e + \frac{\nu}{1 - 2\nu}\epsilon_{kk}^e\delta_{ij}) \quad (26)$$

473 The stress associated to the point force  $\hat{x}$  applied on the surface of normal  $\hat{z}$  at the origin  
 474 is equal at the origin itself to  $\hat{x}\hat{z} + \hat{z}\hat{x}$ .

Since the model treated here is invariant by translation along  $y$ , the force perturbation  $\delta f(u) = \sigma_s^0(\partial_u z)(u)\hat{x}$  is exerted at any  $v \in ]-\infty, \infty[$  and the resulting displacement field at  $(x, y, z)$ , is solely dependent on  $(x, z)$  and can be expressed, by linearity of the elastostatics equations, (similarly to the elastostatic Green function method detailed in Eq.(8.14) by [Landau and Lifchitz, 1986]), as a displacement field  $w$  of components

$$w_i(x, y = 0, z) = \int_{u=-\infty}^{\infty} \int_{v=-\infty}^{\infty} a_i(x - u, -v, z) du dv \delta f(u) \cdot \hat{x} \quad (27)$$

The associated strain perturbation is

$$\epsilon_{ij}^p = \frac{1}{2}(\partial_i w_j + \partial_j w_i), \quad (28)$$

and the associated stress,

$$\sigma_{ij}^1(x) = \frac{E}{1 + \nu}(\epsilon_{ij}^p + \frac{\nu}{1 - 2\nu}\epsilon_{kk}^p\delta_{ij}) + \delta f(x)(\delta_{ix}\delta_{jz} + \delta_{iz}\delta_{jx})\delta(z), \quad (29)$$

where the first term represents the stress induced by the elastic deformation, and the second one the direct application of the force perturbation on the surface. In the above, the spatial derivative of Eq.(28) can be exchanged with the integration in Eq.(27), to

obtain

$$\epsilon_{ij}^p(x, y = 0, z) = \int_{u=-\infty}^{\infty} \int_{v=-\infty}^{\infty} \epsilon_{ij}^e(x - u, -v, z) du dv \delta f(u) \cdot \hat{x}. \quad (30)$$

475 Recalling the expression of the force perturbation, Eq.(8), from Eq.(29), the stress per-  
476 turbation along the surface, at  $z = 0$ , is thus:

$$\begin{aligned} 477 \sigma_{ij}^1(x) &= \sigma_s^0 \cdot p.p. \left[ \int_{u=-\infty}^{\infty} du (\partial_u z)(u) \right. \\ 478 & * \int_{v=-\infty}^{\infty} f_{ij}(x - u, -v, 0) dv \left. \right] \\ 479 & + \sigma_s^0 (\partial_x z)(x) (\delta_{ix} \delta_{jz} + \delta_{iz} \delta_{jx}) \end{aligned} \quad (31)$$

480 where p.p. refers to the principal part of the integral. Taking the derivatives of the  
481 displacement field (equation 25), we can calculate the associated stress. Integrating this  
482 result along the  $y$ -axis gives:

$$483 \int_{v=-\infty}^{\infty} f_{ij}(x, -v, 0) dv = -\frac{2\nu}{\pi x} (\delta_{ix} \delta_{jx} + \delta_{iy} \delta_{jy}) \quad (32)$$

484 and thus,

$$\begin{aligned} 485 \sigma^1(x) &= -\frac{2\nu\sigma_s^0}{\pi} \cdot p.p. \left[ \int_{x'=-\infty}^{\infty} du \frac{(\partial_u z)(u)}{x - u} \right] (\hat{x}\hat{x} + \hat{y}\hat{y}) \\ 486 & + \sigma_s^0 \cdot (\partial_x z)(x) (\hat{x}\hat{z} + \hat{z}\hat{x}) \end{aligned} \quad (33)$$

487 The elastic energy perturbation associated to the interface deformation can be computed  
488 using equation (33) and the relation:

$$489 \sigma^0 = -(p_0 - \sigma_s^0/3)(\hat{x}\hat{x} + \hat{y}\hat{y}) - (p_0 + 2\sigma_s^0/3)\hat{z}\hat{z} \quad (34)$$

490 It results in:

$$\begin{aligned} 491 u_e^1 &= \frac{[(1 + \nu)\sigma_{ij}^0 \sigma_{ij}^1 - \nu\sigma_{kk}^0 \sigma_{ll}^1]}{2E} \\ 492 &= \frac{2\nu[(1 - 2\nu)p_0]}{\pi E} * \sigma_s^0 \cdot p.p. \left[ \int_{u=-\infty}^{\infty} du \frac{(\partial_u z)(u)}{x - u} \right] \end{aligned} \quad (35)$$

## 2.6. Dynamic equation for the dissolution interface

493 The equation (22) rules the dynamics of the interface dissolution. When computed with  
 494 equation (18), it gives:

$$\begin{aligned}
 495 \frac{RT}{k_0\Omega^2}v^1 &= \frac{(\alpha p_0^2 - \alpha_{ref}p_{ref}^2)}{E}\eta(x, z(x)) \\
 496 &\quad -\gamma\partial_{xx}z(x) \\
 497 &\quad +\beta\frac{p_0\sigma_s^0}{E} \cdot p.p. \left[ \int_{u=-\infty}^{\infty} du \frac{(\partial_u z)(u)}{x-u} \right]
 \end{aligned} \tag{36}$$

498 where  $\beta$  is a geometrical factor:

$$499 \beta = [2\nu(1 - 2\nu)]/\pi \tag{37}$$

500 Equation (23) can be expressed in a dimensionless form by using length and time units  
 501 as:

$$502 L^* = \gamma E / (\beta p_0 \sigma_s) \tag{38}$$

$$503 \tau = (L^*)^2 RT / (\gamma k_0 \Omega^2) \tag{39}$$

504 We define the dimensionless variables in the reference frame moving at the average velocity  
 505  $-v_0$  as:

$$506 z' = [z + (v_0 t)] / L^* \tag{40}$$

$$507 x' = x / L^* \tag{41}$$

$$508 t' = t / \tau \tag{42}$$

509 and the reduced quenched noise as:

$$\begin{aligned}
 510 \eta'(x', z'(x, t) - v_0 t / L^*) &= \\
 511 &[(\alpha p_0^2 - \alpha_{ref} p_{ref}^2) / (\beta p_0 \sigma_s)] \eta(x, z(x, t))
 \end{aligned} \tag{43}$$

512 The dimensionless stochastic equation for the stylolite growth process is then:

$$\begin{aligned}
 513 \quad & \partial_{t'} z'(x', t') = \\
 514 \quad & \eta'(x', z'(x', t') - v_0 \tau t' / L^*) + \partial_{x' x'} z' \\
 515 \quad & - p.p. \left[ \int_{u=-\infty}^{\infty} du \frac{(\partial_u z')(u)}{x' - u} \right]
 \end{aligned} \tag{44}$$

516 At large average dissolution speed, the term  $v_0 \tau t' / L^*$  takes over  $z$  quickly and the noise  
 517 is annealed, becoming mostly time-dependent. On the contrary, for sufficiently slow pro-  
 518 cesses such as the extend of the surface roughness over several grains, the noise can be  
 519 considered as quenched. This is the case here as the changes in  $\eta'$  arising from  $z(x, t)$   
 520 are significantly larger than the changes due to some variations of the average dissolution  
 521 front position  $v_0 \tau t' / L^*$ . To the first order, the noise dependence is mainly  $\eta'(x', z'(x', t'))$   
 522 and the noise will therefore be considered here as quenched.

523 The dynamic equation then becomes:

$$\begin{aligned}
 524 \quad & \partial_{t'} z'(x', t') = \eta'(x', z'(x', t')) + \partial_{x' x'} z' \\
 525 \quad & - p.p. \left[ \int_{u=-\infty}^{\infty} du \frac{(\partial_u z')(u)}{x' - u} \right]
 \end{aligned} \tag{45}$$

526 Alternatively, in some arbitrary spatial unit  $\ell$ , this can also be written:

$$527 \quad \partial_t z(x, t) = \eta''(x', z'(x', t')) + \partial_{xx} z - \frac{\ell}{L^*} \int dy \frac{\partial_y z}{x - y} \tag{46}$$

528 with  $L^* = \gamma E / (\beta p_0 \sigma_s)$  and  $\tau = \ell^2 R T / (\gamma k_0 \Omega^2)$ , the time unit.

## 2.7. Small and large scale behavior of the model

529 Elastic interactions can be neglected in equation (46) for small scales such as  $\ell \ll L^*$   
 530 (the lower limit corresponds to the resolution of the analyzed signal) reducing the model

531 to a Laplacian description:

$$532 \quad \partial_t z'(x, t) = \partial_{xx} z' + \eta(x, z'(x)) \quad (47)$$

533 This equation is known as the Edwards Wilkinson model [*Edwards and Wilkinson*, 1982]  
534 modified with a quenched random noise. It has been studied in the literature and leads  
535 to the growth of self-affine surfaces of roughness  $\zeta \sim 1.2$  [*Roux and Hansen*, 1994], in  
536 agreement with existing data on stylolites where  $\zeta \sim 1.1$  [*Schmittbuhl et al.*, 2004].

537 Conversely, for large scales  $\ell \gg L^*$  (the upper limit corresponds to the system size),  
538 surface tension can be neglected reducing equation (46) to a mechanical regime:

$$539 \quad \partial_t z'(x, t) = -\frac{\ell}{L^*} \int dy \frac{\partial_y z}{x - y} + \eta(x, z'(x)) \quad (48)$$

540 In this case, the model is similar to known models describing the propagation of an  
541 elastic line on a disordered pinning landscape or the propagation of a mode I fracture  
542 front in a disordered solid. It leads to the growth of self-affine surfaces of roughness  
543  $\zeta \simeq 0.5$  [*Tanguy et al.*, 1998]. In summary, the model derived above predicts the growth  
544 of dissolution surfaces with different self-affine characteristics at small scale ( $\zeta_1 \sim 1.2$ )  
545 and large scale ( $\zeta_2 \sim 0.5$ ). The transition between these regimes is expected to occur at  
546 a certain cross-over length  $L^*$ .

### 3. Numerical approach : Dynamic evolution of the interface

547 From a purely analytical point of view and via the similarity of asymptotic form of  
548 the dynamic equation with known models for large and small scales, we have shown that  
549 two different scaling laws are expected for small and large scales, and that the cross-over  
550 length should depend on the far-field stress magnitude. Independently from this general  
551 analytical analysis, we will now show how to solve the problem numerically, i.e. implement

552 the dynamic evolution of the interface with all the large and small scale terms and random  
 553 variables to represent the disorder and analyse the resulting morphogenesis.

### 3.1. Practical implementation of the model

554 We simulate the dissolution process for a calcite-water interface. This is done in an  
 555 event-driven discrete lattice code, with algorithms corresponding to a discrete Langevin  
 556 equation leading to grains getting dissolved one at a time: for each grain along the in-  
 557 terface, a time to dissolution is computed from the above Langevin equation, and the  
 558 grain with the shortest dissolution time is removed. After what, the times are recom-  
 559 puted for all grains along the interface, and the next grain with shortest dissolution time  
 560 is removed, and so on (see *Renard et al.* [2004] for details of the practical implementa-  
 561 tion). The selected constants correspond to a calcite-water system,  $\gamma = 0.27 J \cdot m^{-2}$ ,  
 562  $\Omega = 4 \cdot 10^{-5} m^3 \cdot mol^{-1}$ ,  $\nu = 0.25$ ,  $E = 80$  GPa and  $k_0 = 10^{-4} mol \cdot m^{-2} \cdot s^{-1}$  [*Renard et al.*,  
 563 2004]. The chosen physical conditions are  $T = 420$  K,  $\langle p \rangle = 10$  MPa and  $\langle \sigma_s \rangle = 40$   
 564 MPa. The amount of quenched noise is associated to the natural variations of grain prop-  
 565 erties. The typical scale associated to the quenched disorder (or typical grain size) is con-  
 566 sidered here to be around  $\ell = 10 \mu m$ , with no correlation above this scale. This quenched  
 567 disorder has a standard deviation  $\sqrt{\langle \eta^2 \rangle} = [\alpha \ell p_0 / (\beta L^* \sigma_s)] \cdot [(\delta E/E) + (\delta k/k_0) + (\delta \alpha/\alpha)]$   
 568 corresponding to some relative variations of the dissolution rate of around 10% (i.e.  
 569  $\delta k/k_0 \sim 0.1$ ).

570 The dimensionless surface dynamic equation without disorder is:

$$571 \quad \partial_t z(x, t) = v_0 + \partial_{xx} z - \frac{\ell}{L^*} \int dy \frac{\partial_y z}{x - y} \quad (49)$$

572 where  $L^* = \gamma E / (\beta p_0 \sigma_s)$ ,  $\ell$  is the unit length, and  $\tau = \ell^2 RT / (\gamma k \Omega^2)$  is the time unit.

573 We assume a small disorder in the implied quantities (e.g. Young's modulus), that are  
574 quenched in the material properties of the rock heterogeneity associated with micrometric  
575 grains, typically  $\ell = 10\mu\text{m}$ . The interface is supposed to be normal to the largest stress  
576 direction (stabilizing elastic interactions).

577 Considering a perturbation to the first order, in the referential frame of the homo-  
578 geneously moving average front,  $z' = z - v_0t$ , the equation ruling the surface growth  
579 becomes:

$$580 \quad \partial_t z'(x, t) = \partial_{xx} z - \frac{\ell}{L^*} \int dy \frac{\partial_y z}{x - y} + \eta(x, z(x)) \quad (50)$$

581 with a quenched random term  $\eta(x, z'(x)) = [\alpha \ell p_0 / (\beta L^* \sigma_s)] \cdot [(\delta E/E) + (\delta k/k) - (\delta \alpha/\alpha)]$

582 The first and second terms are stabilizing terms. The third term referring to the quenched  
583 disorder destabilizes the interface. We perform the simulation of this dynamic equation  
584 with both stabilizing terms and quenched noise.

585 The prefactors in equation 50 depend on the rock type and on the applied stress. In  
586 addition to these mappings, the characteristic units are known as function of the rock  
587 properties. The cross-over scale  $L^* = \gamma E / (\beta p_0 \sigma_s)$  is function of the pressure during the  
588 growth, through  $p_0$  and  $\sigma_s$ .

589 Determining the cross-over length  $L^*$  for natural samples allows to determine such stress  
590 value during the growth, and consequently the depth of the rock during the stylolite  
591 propagation. Assuming as an order of magnitude  $p_0 \sim \sigma_s$  and typical values for the  
592 limestone elastic properties and the water calcite reaction rates,  $L^* \sim 1\text{mm}$  leads to  
593 a typical depth of 1 km. **Stylolites** can thus be considered as **fossils of the stress**  
594 **magnitude**.

595 We solved the dynamic equation (46) with an event-driven algorithm where the fastest  
596 dissolving grain is removed at each step. The problem is considered as  $L$ -periodic and the  
597 long-range elastic kernel  $p.p. \int dy \frac{\partial_y z}{x-y} = -p.p. \int dy \frac{z(x)-z(y)}{(x-y)^2}$  is replaced by its finite-size form  
598  $-p.p. \int_0^L dy \frac{z(x)-z(y)}{\sin^2(\pi(x-y)/L)} \frac{\pi^2}{L^2}$ . This standard form can be obtained by solving the elastostatic  
599 equations in the Fourier space and performing an inverse Fourier integration. When a new  
600 grain is reached, the realization of its quenched disorder  $\eta$  is evaluated using a Gaussian  
601 distribution. For the dissolution surface simulated which is  $4096\ell$  long, 8000000 grains  
602 were dissolved.

### 3.2. Analysis of the small-scale and large-scale roughness of the saturated interface

603 The simulation of the calcite-water system leads to the growth of a dissolution interface.  
604 Starting from a flat interface and after a certain transient time, the Fourier modes saturate  
605 to a characteristic amplitude. A snapshot of the developed stylolitic interface is shown in  
606 Figure 7.

607 This interface fluctuates around the average progressing flat dissolution front. The  
608 Fourier power spectrum  $P(k, t) = \|\tilde{z}(k, t)\|^2$  of each front  $z(x, t)$  is extracted, and the  
609 ensemble average of this power spectrum  $P(k) = \langle \|\tilde{z}(k)\|^2 \rangle$  is obtained for developed in-  
610 terfaces, by averaging over all fronts after 80000 grains have been dissolved. The expected  
611 small and large scale self-affine characteristics correspond to the theoretical predictions,  
612 as shown in Figure 8. Indeed, the power-spectrum is a power-law of scale, with two dif-  
613 ferent exponents at large and small scale, and a cross-over length around the scale  $L^*$ :  
614 For  $k > 2\pi/L^*$  i.e at small scale, we have  $P(k) \sim k^{-1-2\zeta}$  with  $\zeta_S = 1.2$ , and for the large  
615 scales, the roughness exponent is found to be around  $\zeta_L = 0.35$ . The straight lines in the

616 bilogarithmic axes (Figure 8) correspond to these power law behaviors, determined by  
617 linear regression over the two domains  $k > 2\pi/L^*$  and  $k < 2\pi/L^*$ . The ensemble used for  
618 the roughness estimate is the following: it corresponds roughly to 100000 grain being dis-  
619 solved after the first 80000 first ones, which are discarded. We thus compute the average  
620 power spectral density profiles over all these states, representative of a saturated situation  
621 with fluctuations of the Fourier mode amplitude around some characteristic magnitude for  
622 each wavelength. The linear regression have been performed in bilogarithmic space on  
623 the ranges  $0 < \log_{10}(k) < 1.5$  and  $2 < \log_{10}(k) < 3$ , with  $k$ -unit of  $2\pi/L$ , with  $L = 4096\ell$   
624 and a grain size  $\ell = 10\mu\text{m}$ . The standard error bar provided by the linear regression over  
625 this two ranges is around  $\pm 0.2$  in slope (i.e.  $\pm 0.1$  for the Hurst exponents  $\zeta$ ).

626 Thus, we find that the scaling of saturated surfaces in this model is compatible with  
627 observations made on natural surfaces, and with the previous analytical predictions.

628 In addition, the dynamic behavior of these models (Edwards Wilkinson in a quenched  
629 noise [*Roux and Hansen, 1994*], or elastic string in a disordered landscape [*Tanguy et al.,*  
630 1998]) is known. The prefactor (characteristic time) associated with the dynamics can  
631 be evaluated through the previous computations from the rock material properties. The  
632 time to saturation at an observation scale of a few centimeters is estimated to be around  
633 a few thousands of years. The stylolite roughness is hence always in a saturation state for  
634 a geologist at small observation scale.

635 However, for longer systems, e.g. decametric ones, much longer times would be required  
636 for saturation. Such long stylolites are sometimes observed but rarely analyzed in terms  
637 of scaling of the height. To our knowledge, the only analysis performed on decametric  
638 size stylolites [*Laronne Ben-Itzhak, 2011*] showed that these large scale structures were

639 not saturated. This means that the time during which the stylolitization was active on  
640 such very long stylolites was only enough to lead the small scales to saturated amplitude,  
641 but not the large ones (above a few tenth of centimeters).

#### 4. Example: Application of the model to natural data

642 The model is applied to a sedimentary stylolite collected in a core at the Andra  
643 (French national radioactive waste management agency) Underground Research Labo-  
644 ratory (URL) at Bure in Eastern France. The selected sample comes from the borehole  
645 EST433 at a depth of 720 m. The host rock is a fine-grained, homogeneous grainstone  
646 from the Dogger age. The core was cut in three parts thus giving four profiles for analysis  
647 (Figure 9).

648 Profiles 1 and 2 and profiles 3 and 4 are spaced by 3 mm (thickness of the drilling saw)  
649 and profiles 2 and 3 are spaced by 30 mm. Each profile has a length around 90 mm. The  
650 stylolites were photographed at a resolution of 30  $\mu\text{m}$ . A systematic method was used to  
651 extract profiles from the photographs. It consists on isolating the black pixels constituting  
652 the clay particles in the stylolite from photographs converted in grey level pictures. The  
653 profiles will be used as functions in the spectral analysis (integral transforms) and thus are  
654 required to be single-valued. Stylolites show a self-affinity geometry [*Schmittbuhl et al.*,  
655 1995; *Barabási and Stanley*, 1995] meaning that they are statistically invariant under an  
656 affine transformation. Thus, for  $\Delta x$  and  $\Delta y$  the horizontal direction amplitude and  $\Delta z$  the  
657 vertical direction amplitude:  $\Delta x \rightarrow \lambda \Delta x$ ,  $\Delta y \rightarrow \lambda \Delta y$  and  $\Delta z \rightarrow \lambda^\zeta \Delta z$ , where  $\lambda$  can take  
658 any value and  $\zeta$  is the Hurst exponent which describes the scaling invariance [*Schmittbuhl*  
659 *et al.*, 2004; *Renard et al.*, 2004]. As in *Ebner et al.* [2009b] we used both the Fourier power  
660 spectrum [*Schmittbuhl et al.*, 1995] and the averaged wavelet coefficient [*Simonsen et al.*,

661 1998] signal processing methods to analyse the profiles (Figure 10). We used two different  
662 methods to check the repeatability of the results. First we calculated the Fourier power  
663 spectrum  $P(k)$ , which is the square of the modulus of the Fourier transform, as a function  
664 of the wave-number  $k$  ( $k = 2\pi/L$ , where  $L$  is the wavelength). The power spectrum  
665 expressed as a function of the length for a self-affine profile behaves as  $P(L) \simeq L^{2\zeta+1}$ . We  
666 calculated also the averaged wavelet coefficient spectrum as a function of the scale  $a$  with  
667 Daubechies 4 wavelets which behaves as  $W(a) \simeq a^{1/2+\zeta}$ .

668 The results show the two scaling regimes predicted by the theory presented above,  
669 described by two different power laws. Figure 11 shows the Fourier power spectrum for  
670 the profile 1 as a function of the length  $L$ . The raw data are more concentrated at  
671 small scale. The lower limit for the length corresponds to the Nyquist length which is the  
672 resolution multiplied by 2. As the profiles have a finite-size the upper limit for the analysis  
673 (corresponding to small wave-number) is given by the size of the profile. To analyze the  
674 data, we apply a logarithmic binning so that the weight on each point is equal. To estimate  
675 the cross-over length, we used a linear-by-part fit with a cross-over function changing the  
676 scaling law from small to large scale as explained in *Ebner et al.* [2009b]. The averaged  
677 wavelet coefficient spectrum (Figure 12) does not require a binning. The same kind of  
678 fitting was used to appraise the cross-over length  $L^*$ .

679 The intersection between both regimes (whose slopes are imposed by  $\zeta_S = 1$  and  $\zeta_L = 0.5$   
680 for small and large scale respectively) gives the cross-over length  $L^*$ . We summarize the  
681 estimated cross-over length for all the analyzed profiles with both methods in Table (9).  
682 The uncertainties on the cross-over length (68% and 44% for Fourier power spectrum

683 and averaged wavelet coefficient respectively) are due to the spatial variability of the  
684 intersection between the small and large regimes.

## 5. Discussion

### 5.1. Interpretations of the estimated paleostress

685 We discuss three theories about the meaning of the estimated paleostress for the studied  
686 sedimentary stylolite:

687 • Present day stress: if the conditions for pressure-solution (lithostatic pressure in com-  
688 petition with the presence of a fluid at an appropriate state of equilibrium) are present,  
689 a stylolite should show the present day state of morphology and is still evolving. This  
690 means that we should measure the current applied stress and see the last evolution of  
691 the morphology. This can be compared with recent studies where vertical and horizon-  
692 tal stresses were measured in boreholes at Bure [*Wileveau et al., 2007; Gunzburger and*  
693 *Cornet, 2007*] to assess if the estimated stress corresponds to the measured ones.

694 • Evolution stopped: this can occur if the lithostatic stress becomes too small to  
695 encourage the process (change in the magnitude due to a tectonic phase for example). It  
696 can also be associated with the closing of the porosity by recrystallization. Indeed, if the  
697 pore size decreases because of recrystallization at the pore surface, the surface tension  
698 increases preventing more recrystallization. Thus, the water is getting more charged in  
699 dissolved materials and the chemistry of the water changes and can stop the stylolite  
700 evolution. Moreover, the decrease of the pore size can limit or stop the fluid flow and  
701 close the system.

702 • Reactivation: both previous theories can act on the history of a stylolite. After its  
703 initiation, a stylolite can see its growth stopped by the kind of process we developed

704 just before. If in the geological history an event as emerged soil and/or erosion allows to  
705 change the applied stress or to meteoritic fluids to flow in the soil, the system can have  
706 its properties changed and pressure-solution process can start again until it is stopped or  
707 it can still evolve.

708 These three theories will be discussed with regard to the paleostress results.

## 5.2. Estimation of the paleostresses

### 709 5.2.1. Hypothesis on the basin evolution

710 To estimate the paleostress from the model developed in this study, we use the average  
711 of the cross-over lengths determined for the four profiles. The cross-over length is related  
712 to the stresses by equation (38). However, this equation can be simplified by making  
713 assumptions on the surrounding rock formation. We use the same assumptions as in *Ebner*  
714 *et al.* [2009b] for the stylolites from Cirque de Navacelle (Cévennes, France) considering  
715 that the initiation of stylolites occurs at the early stage of a basin. The major principal  
716 stress is vertical ( $\sigma_{zz}$ ) as we analyzed a sedimentary stylolite. The principal horizontal  
717 stresses are isotropic ( $\sigma_{xx} = \sigma_{yy}$ ). Thus the mean stress  $p_0$  and the shear stress  $\sigma_S$  are:

$$718 \quad p_0 = -(2\sigma_{xx} + \sigma_{zz})/3 \quad (51)$$

$$719 \quad \sigma_S = \sigma_{xx} - \sigma_{zz} \quad (52)$$

720 As stylolites are known to develop in the early stage of sedimentation of basins, the strain  
721 is assumed to be uniaxial:

$$722 \quad \sigma_{xx} = \sigma_{yy} = \frac{\nu}{1 - \nu} \sigma_{zz} \quad (53)$$

723 Using equations (51-53), equation (38) becomes:

$$724 \quad \sigma_{zz}^2 = \frac{\gamma E}{\alpha \beta L^*} \quad (54)$$

725 where

$$726 \quad \alpha = \frac{1(1+\nu)(1-2\nu)}{3(1-\nu)(1-\nu)} \quad (55)$$

727 is a dimensionless geometrical factor. The geometrical factor  $\beta$  (equation 37) is  $\beta =$   
728  $\nu(1-2\nu)/\pi$ . Using the average cross-over length  $\bar{L}^*$  in equation (54), we can estimate  
729 the main principal paleostress  $\sigma_{zz}$ . The Poisson's ratio  $\nu$  of the host rock was determined  
730 by measuring the P and S elastic wave velocities ( $\nu = \frac{0.5(V_P/V_S)^2-1}{((V_P/V_S)^2-1)}$ ). The relative errors  
731 for the measurements of  $V_P$  and  $V_S$  are 1 and 2% respectively [Benson *et al.*, 2005]. The  
732 relative error for the Poisson's ratio is thus equal to 12%. Consequently,  $\alpha$  and  $\beta$  have  
733 error bars equal to 2% and 22%, respectively. The last constant to be determined is the  
734 Young's modulus. The next paragraph details our choices for this matter.

### 735 **5.2.2. Uncertainties on the Young's modulus E**

736 In their paper, Ebner *et al.* [2009b] determined E assuming the vertical stress is equal  
737 to the lithostatic stress as in equation (56) where  $z$  is the current depth of their samples.  
738 They plotted the determined stress as a function of  $L^{-1/2}$ . The slope of the curve is  
739 proportional to  $E^{1/2}$  (see equation (54)). They found  $E = 15$  GPa which is the lowest  
740 acceptable limit for limestones [Clark, 1966]. Based on uniaxial loading made in our  
741 laboratory, we determined  $E = 36.2$  GPa for the rock surrounding the analyzed stylolite.  
742 Considering that the limestones from Bure replaced in the geological context of the Paris  
743 basin cannot be excessively harder than what we observe today, the value determined in  
744 the laboratory is taken as the upper limit for  $E$ . Thus we can estimate the paleostress in  
745 a small range of  $E$ . The values used for the calculation of the paleostress are summarized  
746 in Table (5.2.1).

747 To calculate the paleostress  $\sigma_{zz}$ , we take into account the error bars for each parameter.  
748 The computed error for the calculation of  $\sigma_{zz}$  is 66% for the Fourier power spectrum  
749 method and 54% for the averaged wavelet coefficient method. The results are summarized  
750 in Table (5.2.2).

### 5.3. Geological context

751 By doing some assumptions on the sedimentary overburden, the depth of development  
752 of the stylolite can be assessed. The lithostatic pressure  $\sigma_{zz}$  can be expressed as:

$$753 \quad \sigma_{zz} = \rho gh \quad (56)$$

754 where  $\rho$  is the density in  $g \cdot m^{-3}$ ,  $g$  is the Earth's gravity ( $g = 9.81 m \cdot s^{-2}$ ) and  $h$  is the  
755 depth in  $m$ . We make the assumption that at the initiation of the stylolite, linked to the  
756 early stage of formation of the sedimentary basin, the overburden was made of limestones  
757 only. Thus, we consider the density of limestones  $\rho = 2710 g \cdot m^{-3}$ . The estimated depths  
758 of development of the stylolites are summarized in Figure (12). The error bars on  $h$  are  
759 of the same order as for the paleostress.

760 Now we can wonder what is the interpretation of the estimated paleostress with regard  
761 to the three theories exposed previously:

762 1. *Wileveau et al.* [2007] and *Gunzburger and Cornet* [2007] measured the vertical stress  
763 at Bure which is equivalent to the lithostatic pressure as in equation (56). Our results  
764 show that the calculated depth corresponds to the depth where we cored the analyzed  
765 stylolite. Thus the studied stylolite is more likely to be still active and to show the present  
766 day stress.

767 2. *André et al.* [2010] discussed about a reactivation of the stylolitization during the  
768 Tertiary age (end of Cretaceous more precisely) by the change in the stress orientation  
769 or by the emergence of the Cretaceous sediments which were eroded and permitted to  
770 meteoritic fluid to spread in the sediments. This reactivation process could have acted on  
771 the growth of the studied stylolite until today. But still it seems that the theory of the  
772 present day stress is more applicable on that example.

## 6. Conclusions

773 Analysing the local boundary conditions due to the fact that the inside of a stylolite  
774 does not sustain shear stress and an elastic surrounding, we derived the dependence of  
775 the free energy along a stylolite surface on the shape of the stylolite. Adding up a surface  
776 energy term we derived a dynamic surface evolution model for a stylolitic interface. This  
777 model, in the situation where a stylolite is perpendicular to the largest principal stress axis  
778 - as in most case - includes terms that lead to the stabilization of the surface dynamics,  
779 i.e. to the vanishing of initial perturbations towards a flattening surface. Hence, the  
780 presence of disorder linked to the heterogeneities of the material properties is required to  
781 explain the rough nature of stylolites. Introducing such non correlated quenched disorder,  
782 the model predicts the occurrence of two scaling laws. At small scale, a destabilizing  
783 disorder competing with a stabilizing surface energy term give a model similar to the  
784 Edwards Wilkinson model in a quenched noise leading to a saturated surface with a Hurst  
785 exponent around 1. At large scale, the competition between destabilizing disorder and  
786 stabilizing elastic interactions is similar to models of evolution of an elastic interface in  
787 quenched disorder leading to a Hurst exponent of 0.5.

788 The cross-over scale between these two scaling regimes was shown to be directly linked  
789 to the stress magnitude. Hence, the determination of this cross-over and other physical  
790 rock properties allows to use stylolites as markers of the paleostress magnitude.

791 Both scaling laws and the dependence of this cross-over scale on the stress magnitude  
792 were derived in two ways: by purely analytical derivation and similarity to known models  
793 in section 2 and by numerical integration in section 3.

794 Importantly, it should be noted that the elastic forces, depending on the boundary  
795 conditions, can be stabilizing, as here, or destabilizing. The existence of several models  
796 and techniques of global or local calculation of the free energy can raise the question  
797 of a stabilizing or destabilizing nature of the elastic forces in the context of a stylolite.  
798 Independently from the derivation carried out in details in this paper, we note the following  
799 argument that can distinguish between stabilizing and destabilizing terms. The only  
800 difference between models with stabilizing or destabilizing elastic kernel is the sign of the  
801 prefactor in front of the elastic operator in the dynamic equation. However, when this sign  
802 is reverted, all large scale wavelength Fourier modes become unstable (with a selection of  
803 fastest growing mode, as e.g. shown in *Misbah et al.* [2004] or *Bonnetier et al.* [2009]).  
804 Numerical simulations similar to the ones shown above, with a destabilizing mode, do  
805 not lead to any saturation of the amplitude of the large modes at long times, and the  
806 Fourier power spectrum at a given time does not display any scaling law at fixed time for  
807 the large scales. Thus, the scaling laws observed in field stylolites are compatible with a  
808 model where elastic forces are stabilizing: we take this as a good sign of validity of the  
809 proposed approximations to take the boundary conditions into account in the proposed  
810 model.

811 The results from both analytical and numerical independent resolutions presented in  
812 this study are also consistent with three other independent observations:

813 • The existence of two Hurst exponents at small and large scales, as observed in *Schmit-*  
814 *tbuhl et al.* [2004], in the stylolites from the log cores of Bure (section 4).

815 • The results of recent molecular dynamic models of dissolution with pressure reliance  
816 and surface energy terms in the free energy displaying similar scaling laws and an identical  
817 law for the dependence of the cross-over length over the applied stress [*Koehn*, 2012].

818 • The model was applied in a previous study to stylolites found at various depths in a  
819 limestone formation at Cirques de Navacelles (Cévennes, France). The inferred formation  
820 stresses were compatible with the derived weight of overburden at the time of formation  
821 [*Ebner et al.*, 2009b].

822 We show finally on the example of sedimentary stylolites in Bure, how the confinement  
823 stress can be derived from morphological studies of stylolites. The ubiquitous nature of  
824 these pressure-solution features makes them a versatile marker for paleostress magnitude  
825 that can give access to the stress during the growth of stylolites. This easily available  
826 paleostress marker opens the way for systematic studies of paleostress in large rock for-  
827 mations for different stylolite families. However, it must be used carefully as the error  
828 bars are not minor. An important number of measurement is required to constrain the  
829 results. Together with dating indications for the time of occurrence of such stylolites (as  
830 e.g. times of tectonic events) and current stress assessment methods it opens the way for  
831 the determination of stress evolution in large basins, which is a key to understand their  
832 evolution.

## 7. Acknowledgments

833 We would like to thank C. Aurière, J.D. Bernard, T. Reuschlé, A. Steyer, E. Aharonov,  
834 Y. Bernabé and J.L. Alves for technical help and discussions. This work was partially  
835 funded by the French national radioactive waste management agency (Andra) and sup-  
836 ported by a FORPRO grant. The authors would also like to thank the CAPES-COFECUB  
837 program for stimulating fruitful discussions.

## References

- 838 Aharonov, E., and R. Katsman (2009), Interaction between pressure solution and clays  
839 in stylolite development: insights from modeling, *American J. Sci.*, *309*, 607–632.
- 840 André, G. (2003), *Caractérisation des déformations méso-cénozoïques et des circulations*  
841 *de fluides dans l'Est du Bassin de Paris*, Thesis, Université Henri Poincaré, Nancy,  
842 France.
- 843 André, G., C. Hirsch, S. Fourcade, M. Cathelineau, and S. Buschaert (2010), Chronology  
844 of fracture sealing under a meteoritic fluid environment: microtectonic and isotopic  
845 evidence of major Cainozoic events in the eastern Paris Basin (France), *Tectonophysics*,  
846 *490*, 214–228.
- 847 Angheluta, L., E. Jettestuen, J. Mathiesen, and F. Renard (2008), Stress-driven phase  
848 transformation and the roughening of solid-solid interfaces, *Phys. Rev. Lett.*, (100),  
849 096105.
- 850 Angheluta, L., J. Mathiesen, C. Misbah, and F. Renard (2010), Morphological instabilities  
851 of stressed and reactive geological interfaces, *J. Geophys. Res.*, *115*, b06406.

852 Angheluta, L., E. Jettestuen, and J. Mathiesen (2009), Thermodynamics and roughening  
853 of solid-solid interfaces, *Phys. Rev. E*, *79*(3, Part 1), 031601.

854 Asaro, R., and W. Tiller (1972), Interface morphology development during stress-corrosion  
855 cracking. 1. Via surface diffusion, *Met. Trans.*, *3*, 1789.

856 Barabási, A., and H. Stanley (1995), *Fractal concepts in surface growth*, Cambridge Uni-  
857 versity Press.

858 Bathurst, R. G. C. (1971), *Carbonate sediments and their diagenesis*, Elsevier, Amster-  
859 dam/London/New York.

860 Bathurst, R. G. C. (1987), Diagenetically enhanced bedding in argillaceous platform lime-  
861 stones: stratified cementation and selective compaction, *Sedimentology*, *34*, 749–778.

862 Baud, P., E. Klein, and T. F. Wong (2004), Compaction localization in porous sandstones:  
863 spatial evolution of damage and acoustic emission activity, *J. Struct. Geol.*, *26*, 603–624.

864 Benedicto, A., and R. Schultz (2010), Stylolites in limestones: magnitude of contractional  
865 strain accommodated and scaling relationships, *J. Struct. Geol.*, *32*, 1250–1256.

866 Benson, P. M., P. G. Meredith, E. S. Platzman, and R. E. White (2005), Pore fabric  
867 shape anisotropy in porous sandstones and its relation to elastic wave velocity and  
868 permeability anisotropy under hydrostatic pressure, *Int. J. Rock Mech. Min. Sci.*, *42*,  
869 890–899.

870 Bonnetier, E., C. Misbah, F. Renard, R. Toussaint, and J. Gratier (2009), Does roughening  
871 of rock-fluid-rock interfaces emerge from a stress-induced instability?, *European Phys.*  
872 *J. B.*, *67*, 121.

873 Brouste, A., F. Renard, J. P. Gratier, and J. Schmittbuhl (2007), Variety of stylolites’  
874 morphologies and statistical characterization of the amount of heterogeneities in the

875 rock, *J. Struct. Geol.*, *29*, 422–434.

876 Bushinskiy, G. I. (1961), Stylolites, *Izv. Akad. Nauk. SSSR, Ser. Geophys.*, *8*, 31–46.

877 Buxton, T. M., and D. Sibley (1981), Pressure solution features in a shallow buried  
878 limestone, *J. Sediment. Petrol.*, *51*, 19–26.

879 Clark, S. P. J. (1966), *Handbook of physical constants*, Geological Society of New-York.

880 Cox, M. A., and J. L. Whitford-Stark (1987), Stylolites in the Caballos Novaculite, West  
881 Texas, *Geology*, *15*, 439–442.

882 Cox, S. F., and M. S. Paterson (1991), Experimental dissolution-precipitation creep in  
883 quartz aggregates at high temperatures, *Geophys. Res. Lett.*, *18*, 1401–1404.

884 De Giudici, G. (2002), Surface control vs. diffusion control during calcite dissolution:  
885 Dependence of step-edge velocity upon solution pH, *American Mineralogist*, *87*(10),  
886 1279–1285.

887 Den Brok, S. W. J., and J. Morel (2001), The effect of elastic strain on the microstructure  
888 of free surfaces of stressed minerals in contact with an aqueous solution, *Geophys. Res.*  
889 *Lett.*, *28*, 603–606.

890 Den Brok, S. W. J., and C. Spiers (1991), Experimental evidence for water weakening  
891 of quartzite by microcracking plus solution precipitation creep, *J. Geol. Soc. (London)*,  
892 *148*, 541.

893 Dunnington, H. V. (1954), Stylolite development post-dates rock induration, *J. Sediment.*  
894 *Petrol.*, *24*, 27–49.

895 Dysthe, D., Y. Podlchikov, F. Renard, J. Feder, and B. Jamtveit (2002), Universal scaling  
896 in transient creep, *Phys. Rev. Lett.*, *89*, 246102.

897 Dysthe, D., F. Renard, J. Feder, B. Jamtveit, P. Meakin, and T. Jøssang (2003), High  
898 resolution measurements of pressure solution creep, *Phys. Rev. E*, *68*, 011603.

899 Ebner, M., D. Koehn, R. Toussaint, and F. Renard (2009a), The influence of rock hetero-  
900 geneity on the scaling properties of simulated and natural stylolites, *J. Struct. Geol.*,  
901 *31*, 72–82.

902 Ebner, M., D. Koehn, R. Toussaint, F. Renard, and J. Schmittbuhl (2009b), Stress sen-  
903 sitivity of stylolite morphology, *Earth and Planet. Sci. Lett.*, *277*, 394–398.

904 Ebner, M., R. Toussaint, J. Schmittbuhl, D. Koehn, and P. Bons (2010a), Anisotropic  
905 scaling of tectonic stylolites: a fossilized signature of the stress field, *J. Geophys. Res.*,  
906 *115*, b06403.

907 Ebner, M., S. Piazzolo, F. Renard, and D. Koehn (2010b), Stylolite interfaces and surround-  
908 ing matrix material: Nature and role of heterogeneities in roughness and microstructural  
909 development, *J. Struct. Geol.*, *32*, 1070–1084.

910 Edwards, S. E., and D. R. Wilkinson (1982), The surface statistics of a granular aggregate,  
911 *Proc. R. Soc. London*, *17*.

912 Fabricius, I. L., and M. K. Borre (2007), Stylolites, porosity, depositional texture, and  
913 silicates in chalk facies sediments. Ontong Java Plateau - Gorm and Tyra fields, North  
914 Sea, *Sedimentology*, *54*, 183–205.

915 Fletcher, R. C., and D. D. Pollard (1981), Anticrack model for pressure solution surfaces,  
916 *Geology*, *9*, 419–424.

917 Gonzalez, O., and A. Stuart (2008), *A first course in continuum mechanics*, Cambridge  
918 University Press.

919 Gratier, J. P. (1993), Experimental pressure solution of halite by an indenter technique,  
920 *Geophys. Res. Lett.*, *20*, 1647–1650.

921 Gratier, J. P., and R. Guiguet (1986), Experimental pressure solution-deposition on quartz  
922 grains: the crucial effect of the nature of the fluid, *J. Struct. Geol.*, *8*, 845–856.

923 Gratier, J. P., L. Jenatton, D. Tisserand, and R. Guiguet (2004), Indenter studies of the  
924 swelling, creep and pressure solution of Bure argillite, *App. Clay Sci.*, *26*, 459–472.

925 Gratier, J. P., L. Muquet, R. Hassani, and F. Renard (2005), Experimental microstylolites  
926 in quartz and modeled application to natural stylolitic structures, *J. Struct. Geol.*, *27*,  
927 89–100.

928 Grinfeld, M. A. (1986), Instability of the interface between a nonhydrostatically stressed  
929 elastic body and a melt, *Sov. Phys. Dokl.*, *31*, 831.

930 Gunzburger, Y., and F. H. Cornet (2007), Rheological characterization of a sedimentary  
931 formation from a stress profile inversion, *Geophys. J. Int.*, *168*, 402–418.

932 Heald, M. T. (1955), Stylolites in sandstones, *J. Geol.*, *63*, 101–114.

933 Iijima, A. (1979), Nature and origin of the Paleogene cherts in the Setogawa Terrain,  
934 Shizuoka, central Japan, *J. Fac. Sci. Univ. Tokyo, Sect. 2*, *20*, 1–30.

935 Karcz, Z., E. Aharonov, D. Ertas, R. Polizzotti, and C. H. Scholz (2008), Deformation by  
936 dissolution and plastic flow of a single crystal sodium chloride indenter: an experimental  
937 study under the confocal microscope, *J. Geophys. Res.*, *113*, b04205.

938 Kassner, K., C. Misbah, J. Müller, J. Kappey, and P. Kohlert (2001), Phase-field modeling  
939 of stress-induced instabilities, *Phys. Rev. E*, *63*, 036117.

940 Katsman, R. (2010), Extensional veins induced by self-similar dissolution at stylolites:  
941 analytical modeling, *Earth and Planet. Sci. Lett.*, *299*, 33–41.

942 Katsman, R., E. Aharonov, and H. Scher (2006a), A numerical study on localized volume  
943 reduction in elastic media: some insights on the mechanics of anticracks, *J. Geophys.*  
944 *Res.*, *111*, b03204.

945 Katsman, R., E. Aharonov, and H. Scher (2006b), Localized compaction in rocks: Esh-  
946 lley's inclusion and the Spring Network Model, *Geophys. Res. Lett.*, *33*, 110311.

947 Koehn, D. (2012), personal comm.

948 Koehn, D., J. Arnold, B. Jamtveit, and A. Malthe-Sørenssen (2003), Instabilities in stress  
949 corrosion and the transition to brittle failure, *American J. Sci.*, *303*, 956–971.

950 Koehn, D., D. K. Dysthe, and B. Jamtveit (2004), Transient dissolution patterns on  
951 stressed crystal surfaces, *Geochimica et Cosmochimica Acta*, *68*, 3317–3325.

952 Koehn, D., F. Renard, R. Toussaint, and C. W. Passchier (2007), Growth of stylolite  
953 teeth patterns depending on normal stress and finite compaction, *Earth and Planet.*  
954 *Sci. Lett.*, *257*, 582–595.

955 Landau, L. D., and E. M. Lifchitz (1986), *Theory of elasticity*, Butterworth-Heinemann-  
956 London, 3rd ed.

957 Laronne Ben-Itzhak, L. (2011), *Pressure solution and stylolites in carbonate rocks*, *Ph.D.*  
958 *dissertation thesis*, Weizmann Institute of Sciences, Rehovot.

959 Lind, I. L. (1993), Stylolites in chalk from leg 130, Ontong Java Plateau, *Proc. ODP Sci.*  
960 *Results*, *130*, 673–686.

961 Misbah, C., F. Renard, J. P. Gratier, and K. Kassner (2004), Dynamics of a dissolution  
962 front for solids under stress, *Geophys. Res. Lett.*, *31*, 106618.

963 Mollema, P. N., and M. A. Antonellini (1996), Compaction bands: a structural analog for  
964 anti-mode I crack in aeolian sandstone, *Tectonophysics*, *267*, 209–228.

965 Park, W. C., and E. H. Schot (1968), Stylolites: their nature and origin, *J. Sediment.*  
966 *Petrol.*, *38*, 175–191.

967 Railsback, L. B. (1993), Lithologic controls on morphology of pressure-dissolution surfaces  
968 (stylolites and dissolution seams) in Paleozoic carbonate rocks from the mideastern  
969 United States, *J. Sed. Res.*, *63*, 513–522.

970 Renard, F., P. Ortoleva, and J. P. Gratier (1997), Pressure solution in sandstones: influ-  
971 ence of clays and dependence on temperature and stress, *Tectonophysics*, *280*, 257–266.

972 Renard, F., D. Dysthe, J. Feder, K. Bjørlykke, and B. Jamtveit (2001), Enhanced pressure  
973 solution creep rates induced by clay particles: experimental evidence in salt aggregates,  
974 *Geophys. Res. Lett.*, *28*, 1295–1298.

975 Renard, F., J. Schmittbuhl, J. P. Gratier, P. Meakin, and E. Merino (2004), Three-  
976 dimensional roughness of stylolites in limestones, *J. Geophys. Res.*, *109*, b03209.

977 Rispoli, R. (1981), Stress field about strike-slip faults inferred from stylolites and tension  
978 gashes, *Tectonophysics*, *75*, 29–36.

979 Roux, S., and A. Hansen (1994), Interface roughening and pinning, *J. Phys. I (France)*,  
980 *4*, 515–538.

981 Rutter, E. H. (1976), The kinetics of rock deformation by pressure solution, *Philos. Trans.*  
982 *R. Soc. London Ser.A*, *283*, 203–219.

983 Rutter, E. H. (1983), Pressure solution in nature, theory and experiment, *J. Geol. Soc.*,  
984 *140*, 725–740.

985 Schmittbuhl, J., F. Schmitt, and C. Scholz (1995), Scaling invariance of crack surfaces, *J.*  
986 *Geophys. Res.*, *100*, 5953–5973.

987 Schmittbuhl, J., F. Renard, J. P. Gratier, and R. Toussaint (2004), Roughness of stylolites:  
988 implications of 3D high resolution topography measurements, *Phys. Rev. Lett.*, *93*,  
989 238501.

990 Schutjens, P., and C. Spiers (1999), Intergranular pressure solution in NaCl: Grain-to-  
991 grain contact experiments under the optical microscope, *Oil Gas Sci. Technol.*, *54*, 729.

992 Simonsen, I., A. Hansen, and O. M. Nes (1998), Determination of the Hurst exponent by  
993 use of wavelet transforms, *Phys. Rev. E*, *58*, 2779–2787.

994 Stockdale, P. B. (1922), Stylolites: their nature and origin, *Indiana University Studies*, *9*,  
995 1–97.

996 Stockdale, P. B. (1926), The stratigraphic significance of solution in rocks, *J. Geol.*, *34*,  
997 399–414.

998 Stockdale, P. B. (1936), Rare stylolites, *American J. Sci.*, *32*, 129–133.

999 Stockdale, P. B. (1943), Stylolites: primary or secondary?, *J. Sediment. Petrol.*, *13*, 3–12.

1000 Stutzer, O. (1940), *Geology of coal*, Univ. Chicago Press.

1001 Tanguy, A., M. Gounelle, and S. Roux (1998), From individual to collective pinning:  
1002 Effect of long-range elastic interactions, *Phys. Rev. E*, *58*, 1577–1590.

1003 Tembe, S., P. Baud, and T. Wong (2008), Stress conditions for the propagation of discrete  
1004 compaction bands in porous sandstone, *J. Geophys. Res.*, *113*, b09409.

1005 Wileveau, Y., F. H. Cornet, J. Desroches, and P. Blumling (2007), Complete in situ stress  
1006 determination in an argillite sedimentary formation, *Phys. Chem. Earth*, *32*, 866–878.

1007 Wright, T. O., and L. B. Platt (1982), Pressure dissolution and cleavage in Martingsburg  
1008 shale, *American J. Sci.*, *282*, 122–135.

1009 Young, R. B. (1945), Stylolitic solution in Wit-watersrand quartzites, *Geol. Soc. S. Afr.*  
1010 *Trans.*, 47, 137–142.

1011 Zhou, X., and A. Aydin (2010), Mechanics of pressure solution seam growth and evolution,  
1012 *J. Geophys. Res.*, 115, b12207.

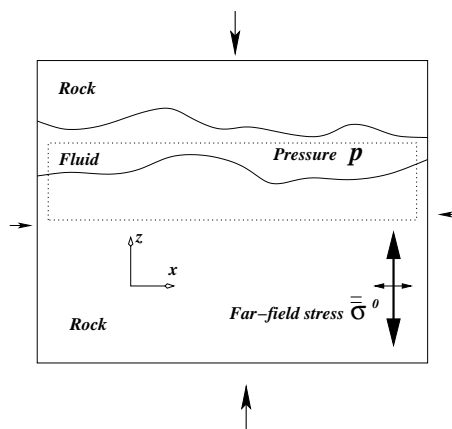


**Figure 1.** Initial stage of a stylolite: Trapped elongated fluid pocket.

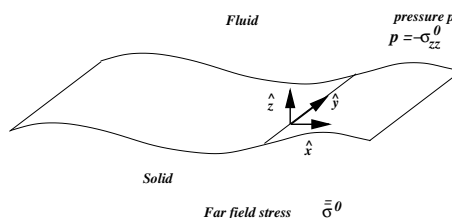


**Figure 2.** Solid-fluid interface: geometry considered.

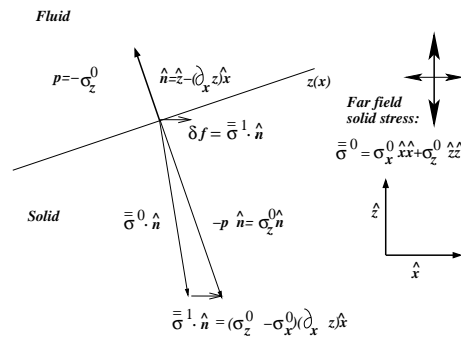


**Figure 3.** Local mechanical equilibrium along the fluid-solid interface (equation 8).

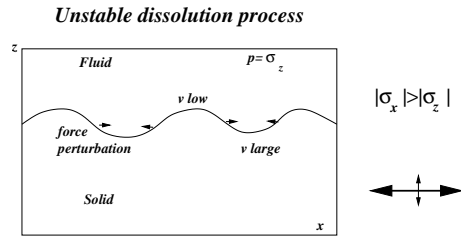


**Figure 4.** Surface tangential to the largest stress ( $\sigma_{xx}$ ) axis: unstable case, Azaro-Tiller-Grinsfeld instability.

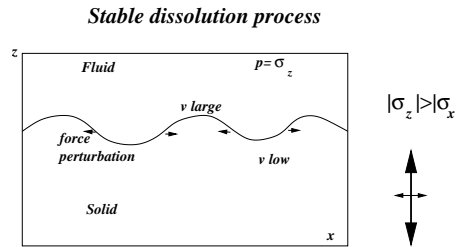


**Figure 5.** Surface normal to the largest stress ( $\sigma_{zz}$ ) axis: stable case.

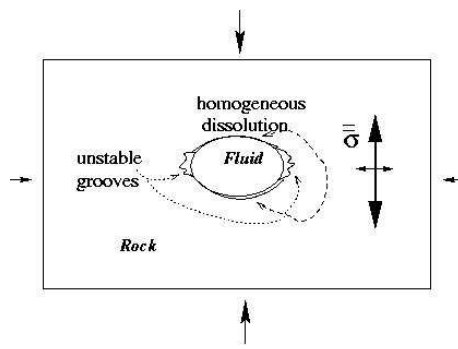


**Figure 6.** Expected stability or instability of the dissolution front around a trapped fluid pocket.

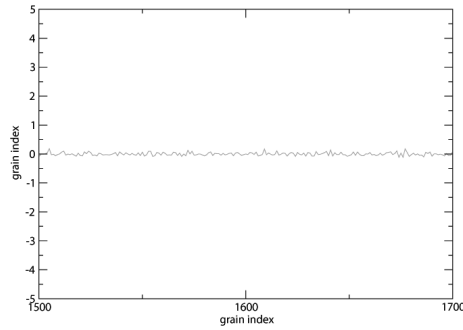


**Figure 7.** Snapshot of the pressure-solution profile.

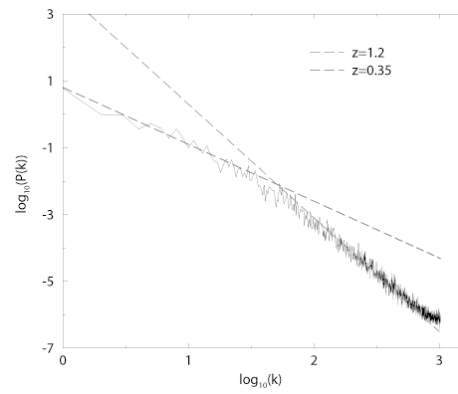


**Figure 8.** Average power spectrum of simulated stylolitic fronts, in bilogarithmic representation. The  $k$ -unit is  $2\pi/L$ , with  $L = 4096\ell$  and a grain size  $\ell = 10\mu\text{m}$ . The vertical unit is arbitrary. The crossover is obtained at  $2\pi/L^*$ .

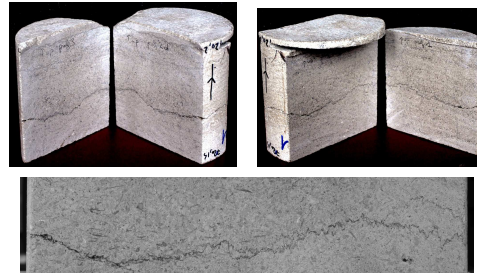


**Figure 9.** Profiles 1, 2, 3 and 4 from right to left. A core from the Dogger formation (EST433 well) was cut in three parts to obtain four profiles. Each profile was photographed at high resolution. The picture at the bottom shows the profile number 2.

Profile number	1	2	3	4	Average, $\bar{L}^*$
$L_{FPS}^*$ (mm)	1.14	0.37	0.37	1.13	$0.75 \pm 0.51$
$L_{AWC}^*$ (mm)	1.95	1.52	0.72	1.60	$1.45 \pm 0.64$

**Table 1.** Summary of the cross-over length found for the four profiles analyzed by Fourier power spectrum (FPS) and average wavelet coefficient (AWC).

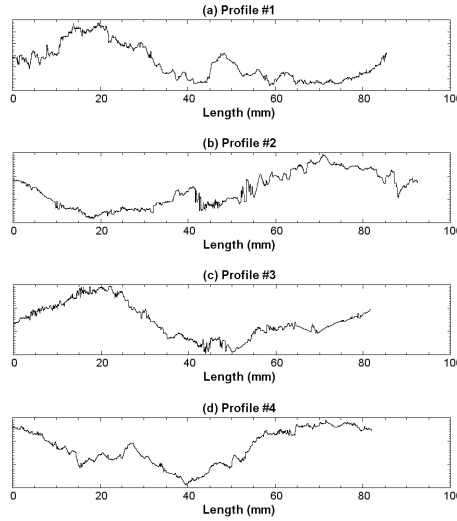


**Figure 10.** Functions obtained from profiles 1, 2, 3 and 4. A grey-level threshold was imposed on the pictures to isolate the stylolites. The functions were then obtained by selecting the mean limit of the pixels.

$\gamma(J \cdot m^{-2})$	$E_{up}(GPa)$	$\nu$	$\alpha$	$\beta$
0.27	$36.2 \pm 0.4$	$0.37 \pm 0.04$	$0.32 \pm 0.01$	$0.033 \pm 0.007$

**Table 2.** Summary of the estimated paleostress for the stylolites from the cross-over length.

Paleostress (MPa)	$\bar{L}^*, E_{low}$	$\bar{L}^*, E_{up}$
$\sigma_{FPS}$	$22.6 \pm 14.9$	$35.1 \pm 23.2$
$\sigma_{AWC}$	$16.3 \pm 8.8$	$25.3 \pm 13.7$

**Table 3.** Results for the calculation of the paleostress  $\sigma_{zz}$  using the averaged cross-over length for the Fourier power spectrum (FPS) and average wavelet coefficient (AWC) methods. We calculated the paleostress taking into account the variability of the Young's modulus  $E$  where  $E_{low}$  is the lower limit for the Young's modulus for limestones and  $E_{up}$  is the determined Young's modulus for the studied sample.

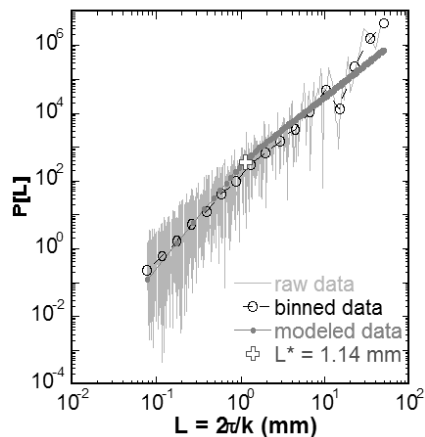


**Figure 11.** Fourier power spectrum of the profile 1. The raw data were binned logarithmically to run a linear-by-part fitting on the data [Ebner *et al.*, 2009b]. Two different scaling regimes are observed at small and large scale with Hurst exponent around 1 and 0,5 respectively. The fit reveals a cross-over length  $L^*$  around 1.14 mm.

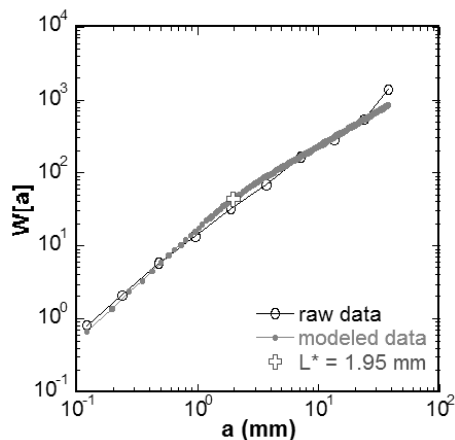


**Figure 12.** Averaged wavelet coefficient spectrum of the profile 1. A linear-by-part fitting were run on the data [Ebner *et al.*, 2009b]. Two different scaling regimes are observed at small and large scale with Hurst exponent around 1 and 0.5 respectively. The fit reveals a cross-over length  $L^*$  around 1.95 mm. This is in good agreement with the length inferred using the Fourier power spectrum method.

Depth (m)	$\bar{L}^*, E_{low}$	$\bar{L}^*, E_{up}$
$h_{FPS}$	850.1±561.1	1320.3±871.4
$h_{AWC}$	613.1±331.1	951.7±513.9

**Table 4.** Results for the calculation of the depth for the Fourier power spectrum (FPS) and average wavelet coefficient (AWC) methods. We consider an early stage of formation of a sedimentary basin with an overburden made of limestones only.